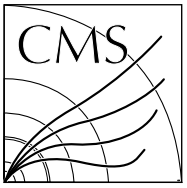

The Compact Muon Solenoid Experiment

CMS Note

Mailing address: CMS CERN, CH-1211 GENEVA 23, Switzerland

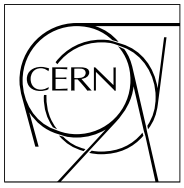

24 July, 2006

Potential to Discover Supersymmetry in Events with Muons, Jets and Missing Energy in pp Collisions at $\sqrt{s} = 14$ TeV with the CMS Detector

Yu. Pakhotin[*)], B. Scurlock[*)], D. Acosta, P. Bartalini, R. Cavanaugh, A. Drozdetskiy, A. Korytov, K. Kotov, K. Matchev, G. Mitselmakher, M. Schmitt

Institute for High Energy Physics and Astrophysics, University of Florida, Gainesville, Florida, U.S.A.

Abstract

Generic signatures of supersymmetry with R-parity conservation include those of single isolated muons or like-sign isolated dimuon pairs, accompanied with energetic jets and missing transverse energy. The ability of CMS to discover supersymmetry with these signals is estimated for 10 fb^{-1} of data collected with the inclusive single-muon and dimuon High-Level-Trigger paths. The selection criteria are optimized and the systematic effects are studied for a single low-mass benchmark point of the constrained MSSM with $m_0 = 60\,\text{GeV}/c^2$, $m_{1/2} = 250\,\text{GeV}/c^2$, $\tan\beta = 10$, $A_0 = 0$ and $\mu > 0$. Discovery contours in the (m_0, $m_{1/2}$) plane are presented for integrated luminosities ranging from 1 to 100 fb^{-1}.

[*)] Contact persons. e-mail: pakhotin@phys.ufl.edu, bslock@phys.ufl.edu

1 Introduction

Low energy supersymmetry is a promising candidate for new physics beyond the Standard Model. In a large class of supersymmetric models studied, the superpartners carry a conserved quantum number, R-parity, which guarantees that the lightest supersymmetric particle (LSP) is stable. It also implies that superpartners are pair produced at colliders. Supersymmetric particle decays are typically prompt, and decay cascades always end up with the LSP. Because the LSP has to be neutral and colourless to satisfy cosmological constraints [1], the generic collider signatures involve large missing energy carried away by the two undetected LSP's together with other prompt observable objects such as jets and leptons.

The work presented in this note is carried out in the framework of the CMSSM [2], i.e., the minimal supersymmetric extension to the standard model, further constrained by grand unification relations (GUT), and described by only five parameters at the GUT scale: a universal gaugino mass $m_{1/2}$, a universal scalar mass m_0, the ratio of the vacuum expectation values of the two Higgs doublets $\tan\beta$, a universal trilinear scalar coupling A_0 and the sign of the Higgs mixing mass term μ.

Small $m_{1/2}$ values have already been excluded (Fig. 1) by LEP searches [3] for Higgs bosons [4] and for charginos[5] and neutralinos [6]. While the Tevatron searches [7] do not have the sensitivity to extend LEP results in the CMSSM, the larger centre-of-mass energy and luminosities that will be made available at the LHC will allow a much larger domain of the parameter space to be covered. Owing to the ability of the CMS detector to identify and reconstruct muons with good efficiency [8], the analyses presented here address the topologies with either at least one muon or a like-sign dimuon pair, accompanied with energetic jets and large transverse missing energy ($E_T^{\rm miss}$). These signatures are experimentally clean when compared to that involving only jets and missing energy, and have the anticipated advantage of an efficient and well-understood trigger shortly after LHC start-up. The analysis with two same-sign muons is complementary to trilepton searches because it involves more diagrams [9, 10, 11, 12].

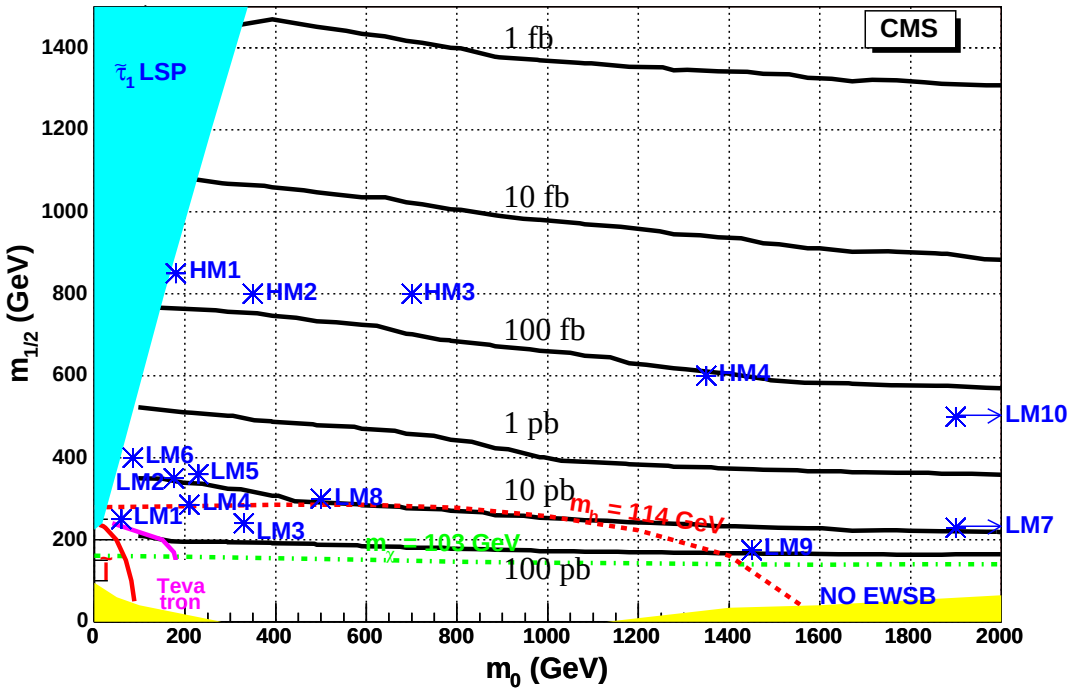

Figure 1: Total SUSY production cross section in the $(m_0, m_{1/2})$ parameter plane of the CMSSM. Other CMSSM parameters are fixed: $\tan\beta = 10$, $A_0 = 0$ and $\mu > 0$. CMSSM benchmark points are shown as stars (LM2, LM8 and HM2 have different CMSSM parameters as shown in Table 1). Regions excluded by theory (charged LSP and no electroweak symmetry breaking — shaded areas) are also shown. The region already excluded by the direct searches for squarks and gluinos at the Tevatron is delineated by the light (magenta) solid curve. The region already excluded by the direct searches for sleptons at LEP is delineated by the dark (red) solid curve. The dashed and dash-dotted lines indicate the regions of the parameter plane for which the Higgs boson mass is smaller than 114 GeV/c^2 and the lighter chargino mass is smaller than 103 GeV/c^2, hence giving a good approximation of the LEP-excluded domains.

This work is organized as follows: the features of the CMS detector relevant for this study are briefly summarized

in Section 2. The signal and background samples, as well as the detector simulation procedures, are listed in Section 3. The trigger path, the physics object reconstruction, and the event pre-selection in both the single muon and dimuon final states are described in turn in Section 4. The strategy developed to optimize the selection cuts in both analyses is presented in Section 5. Systematic uncertainties are dealt with in Section 6 and the results of both analyses are shown in Section 7. Appendices contain detailed information about the event samples generated, the selection cut efficiencies, and a comparison between fast and full simulations.

2 The CMS Detector

The Compact Muon Solenoid (CMS) is a multi-purpose, nearly 4π-solid-angle-coverage detector [8, 13], which is being constructed at the future Large Hadron Collider (LHC) located at CERN near Geneva, Switzerland.

The guiding design principle of CMS involves a $4\,\mathrm{T}$ superconducting solenoid [14] which enables the construction of a relatively compact muon spectrometer, capable of detecting and reconstructing muons with good precision and efficiency for muon momentum transverse to the beam (p_T) in excess of $\sim 1\,\mathrm{TeV}/c$. Inside the solenoid and immersed in the $4\,\mathrm{T}$ axial magnetic field, a pixel detector combined with a silicon strip tracker [15] enable the charged particle trajectories to be reconstructed and their momenta to be measured.

A lead-tungstate crystal electromagnetic calorimeter (ECAL) [16] surrounds the inner tracking volume and a brass-scintillator tile hadron calorimeter (HCAL) [17] envelops the ECAL. The HCAL provides hermetic coverage up to $|\eta| = 5$, important for missing energy measurements. The combined calorimeter system allows jets to be reconstructed with an effective stochastic resolution term of approximately $125\%/\sqrt{E_T}$ and a small constant term of approximately 3.3%. Similarly, the missing transverse energy is expected to be reconstructed with an effective stochastic uncertainty term of approximately $123\%\sqrt{\Sigma E_T}$ (where ΣE_T is the scalar sum of the transverse energy over all calorimeter towers) [8].

The muon system [18] lies outside the solenoid volume and is composed of three different detector types: drift tubes (DT) are located in the barrel region, cathode strip chambers (CSC) are located in the end-cap regions up to $|\eta| = 2.4$, and resistive plate chambers (RPC), used for fast triggering, are located throughout the barrel and end-caps. The muon system provides a reconstruction efficiency in excess of 95%.

3 Event Simulation

In this work, the response of the detector to incident particles is simulated using a GEANT4-based framework [19], known as the Object-oriented Simulation for CMS Analysis and Reconstruction (OSCAR) [8]. The inclusion of pile-up and the reconstruction of analysis objects (muons, jets, etc) from hits in the detector is performed by a software framework known as the Object-oriented Reconstruction for CMS Analysis (ORCA) [8]. In addition, a standalone fast simulation, known as the CMS FAst MOnte Carlo Simulation (FAMOS) framework [8], is used in this work to facilitate simulations involving CMSSM parameter scans.

In both the full and fast simulations, hits from minimum bias events are superimposed on the main simulated event to reproduce the pile-up conditions expected for a luminosity of $2 \times 10^{33}\mathrm{cm}^{-2}\mathrm{s}^{-1}$.

3.1 Signal from Supersymmetry

The supersymmetric particle couplings and masses are calculated by ISASUGRA 7.69 which is part of the event generator ISAJET 7.69 [20]. Cross sections and decay widths are then derived by PYTHIA 6.225 [21]. The library CTEQ5L [22] is used for the parton distribution functions. The different parameters for all fully simulated SUSY points used in this note are listed in Table 1. The total expected cross section from supersymmetry is also displayed in Fig. 1 as a function of m_0 and $m_{1/2}$, for $\tan\beta = 10$, $A_0 = 0$ and $\mu > 0$.

A scan of the $(m_0, m_{1/2})$ plane with a (100 GeV/c^2, 100 GeV/c^2) grid is performed with the fast simulation, for $\tan\beta = 10$, $A_0 = 0$ and $\mu > 0$. For comparison, validation and efficiency calibration purposes, several of the benchmark samples of Table 1 are also processed with the fast simulation. The LM1 benchmark point is chosen for selection optimization in this study.

3.2 Standard Model Backgrounds

Several standard model processes contribute to final states with at least one muon accompanied by multiple jets and missing energy. The main backgrounds studied in this analysis, summarized in Appendix A, are multi-jet QCD

Table 1: Parameters of fully simulated and reconstructed SUSY benchmark points studied in this work. The number of simulated events is given by $N_{\texttt{Gen}}$ and the equivalent integrated luminosity is given by L.

	m_0 (GeV/c^2)	$m_{1/2}$ (GeV/c^2)	$\tan\beta$	A_0	$\texttt{sign}(\mu)$	$\sigma_{\texttt{LO}}$ (pb)	$N_{\texttt{Gen}}$	L (fb^{-1})
LM1	60	250	10	0	+	41.9	98250	2.3
LM2	185	350	35	0	+	7.4	93000	12.6
LM4	210	285	10	0	+	19	96500	5.1
LM5	230	360	10	0	+	6	84000	13.9
LM6	85	400	10	0	+	4	99250	24.6
LM7	3000	230	10	0	+	10.2	7500	0.7
LM8	500	300	10	-300	+	8.8	58250	6.6
LM10	3000	500	10	0	+	0.178	19750	110.7
HM1	180	850	10	0	+	0.052	80000	1538.5
HM2	350	800	35	0	+	0.068	28500	419.2

production, $\mathrm{t\bar{t}}$ QCD production, and single-boson and diboson electroweak production.

Because full next-to-leading (NLO) calculations do not yet exist for all background processes, this work uses only leading order (LO) cross sections, consistently for both signal and all backgrounds. Further, PYTHIA is used to simulate all background processes studied in this work. Because the PYTHIA parton shower model for initial/final state radiation (ISR/FSR) is only realistic in the collinear approximation, the effect of high E_T jets from ISR/FSR can be significantly underestimated in the backgrounds used by this study. Generators such as ALPGEN [23] and MC@NLO [24], which use a matrix element approach, provide a more realistic description of ISR/FSR jets but are beyond the scope of this work. A systematic uncertainty representing the difference between the parton shower model and the matrix element approach is estimated in Section 6.

3.2.1 Multi-jet QCD Production

Multi-jet QCD events do not intrinsically involve Feynman diagrams with final states similar to the topological signature required by this analysis. Owing to its enormous cross section ($\sigma_{\mathrm{jj}} \sim 55\,\mathrm{mb}$), however, multi-jet events can produce configurations which are experimentally close. For example, in addition to multiple jets, significant missing transverse energy can be faked by mis-measurement of jet energies. Similarly, muons can be produced in heavy flavour events, hence accompanied with $\not\!\!E_T^{\mathrm{miss}}$, or faked in several ways such as punch-through or charged pion/kaon decays.

The number of multi-jet events expected for integrated luminosity of $10\,\mathrm{fb}^{-1}$ (Fig. 2 and Appendix A) is so large at small $\hat{p}_T$ (defined as the transverse momentum of one of the two original hard scattered partons) that it is practically impossible to generate and simulate such a large amount of events. Consequently, events were generated almost uniformly in not less than 21 $\hat{p}_T$ bins (Fig. 2) and are given a weight equal to the ratio of the number of events expected to that actually generated in the corresponding bin.

3.2.2 Top Production

Another particularly important source of background is $\mathrm{t\bar{t}}$ QCD production, due to its modestly large cross section $\sigma_{\mathrm{t\bar{t}}} \sim 490\,\mathrm{pb}$ and its intrinsic multi-jet, high missing transverse energy, and significant leptonic final state nature. A total of approximately 3.4 million $\mathrm{t\bar{t}}$ events (corresponding to an equivalent integrated luminosity of $6.9\,\mathrm{fb}^{-1}$) were simulated and used in this analysis, as shown in Appendix A.

3.2.3 Single-boson electroweak production (with jets)

The production of single W and Z bosons is expected to be plentiful at the LHC due to their high cross sections, $\sigma_{\mathrm{W}} \sim 1.2 \times 10^5\,\mathrm{pb}$ and $\sigma_{\mathrm{Z}} \sim 3.3 \times 10^4\,\mathrm{pb}$. Because it is nearly impossible to generate and simulate all the needed events for integrated luminosity of $10\,\mathrm{fb}^{-1}$, the single-boson electroweak events (Fig. 3 and Appendix A) were generated uniformly in $20\,\hat{p}_T$ bins, and are given a weight equal to the ratio of the number of events expected to that actually generated in the corresponding bin.

Jets accompany single W and Z production due to, for example, t-channel-like ISR/FSR diagrams where one outgoing leg is the W or Z and the other outgoing leg is a radiated gluon. As noted earlier, because the PYTHIA

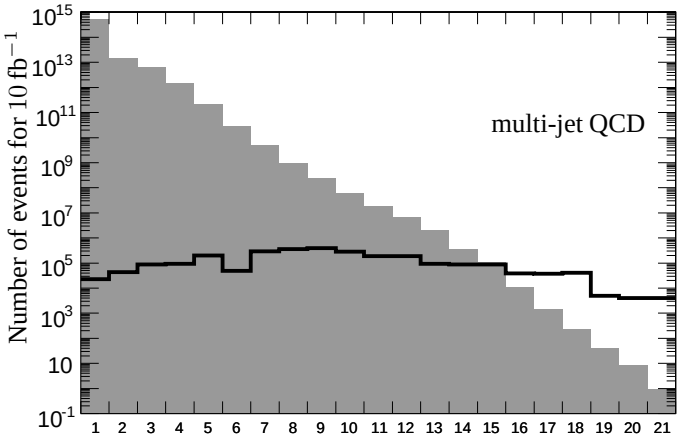

Figure 2: Numbers of multi-jet QCD events expected for integrated luminosity of $10\,\mathrm{fb}^{-1}$ (shaded area), and numbers of events produced (full curve) as a function of $\hat{p}_T$. More details may be found in Appendix A

.

parton shower model for initial/final state radiation is only realistic in the collinear approximation, the effect of high E_T jets from ISR/FSR can be significantly underestimated for this type of background. A systematic uncertainty representing the difference between the parton shower model and the matrix element approach is estimated in Section 6.

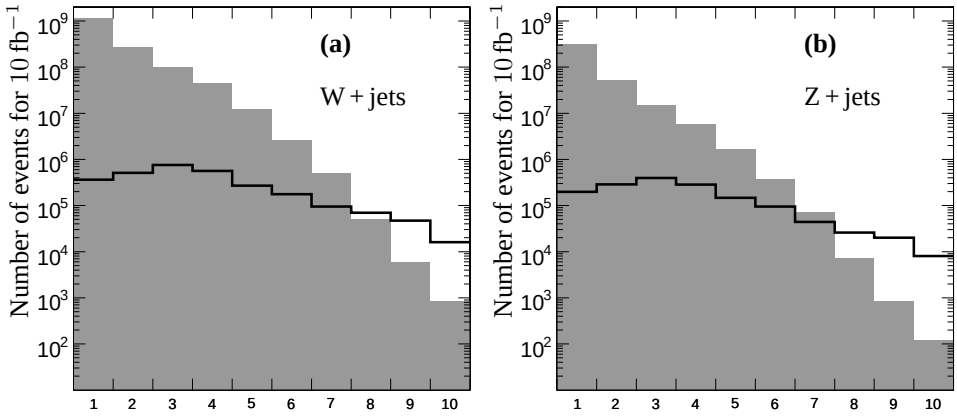

Figure 3: Left plot (a) shows numbers of W + jets events expected for integrated luminosity of $10\,\mathrm{fb}^{-1}$ (shaded area), and numbers of events produced (full curve) as a function of $\hat{p}_T$. Right plot (b) shows numbers of Z + jets events expected for integrated luminosity of $10\,\mathrm{fb}^{-1}$ (shaded area), and numbers of events produced (full curve) as a function of $\hat{p}_T$. More details may be found in Appendix A.

The primary contribution of W + jets as a background process to this study is due to leptonic decays of the W into a muon and a neutrino, thus mimicking the muon-plus-missing-energy-plus-jets signature of the signal. The primary contribution of Z + jets is due to leptonic decays of the Z into dimuons, ditaus, or neutrino pairs, leading to large E_T^{miss} (as measured in the calorimeters) accompanied by jets. The numbers of fully simulated and reconstructed electroweak single-boson events used in this work may be found in Appendix A.

3.2.4 Diboson electroweak production (with jets)

Diboson production, such as WW + jets, WZ + jets, and ZZ + jets, also contributes as a source of background to this study, due to the existence of several final states involving muons, jets and large E_T^{miss}. Because of the additional weak vertex, the cross sections, while significant with respect to this study, are much less than for single-boson production: $\sigma_{\mathrm{WW}} \sim 190\,\mathrm{pb}$, $\sigma_{\mathrm{WZ}} \sim 27\,\mathrm{pb}$ and $\sigma_{\mathrm{ZZ}} \sim 10\,\mathrm{pb}$. The numbers of fully simulated and reconstructed electro-weak diboson events used in this work may be found in Appendix A.

4 Online and Event Pre-selection

Event selection is performed at two levels: online selection at the trigger level and offline selection at the analysis level. The algorithms to reconstruct the physical objects (muon, jets, etc) as well as their identification at the online and offline levels are described in Ref. [8]. The online selection and the offline pre-selection pertaining to the single-muon and dimuon analyses are summarized below.

4.1 Trigger

The trigger is composed of a hardware-based Level-1 (L1) Trigger system [25] and a software-based High-Level Trigger (HLT) system [26]. The latter is often subdivided into so-called Level-2 (L2) and Level-3 (L3) triggers, which simply refer to the level of sophistication of the reconstructed objects available at a given time, but which do not correspond to any real structure. The event rate is reduced at Level-1 to $50\,$kHz, whilst the HLT uses the reconstructed object information to further reduce the event rate to $100\,$Hz written to mass storage. This work uses event samples selected by two HLT triggers, the inclusive single-muon and the dimuon triggers.

Muon candidates are formed at Level-2 of the High-Level Trigger as follows. In the endcaps, a RPC track must be reconstructed and matched with a CSC track from the L1. In the barrel, at least one DT track segment must be reconstructed and be associated with at least four RPC hits. In both the endcap and barrel cases, the L2 muon candidate is required to be compatible with originating from the collision vertex in the plane transverse to the beam. At Level-3 of the High-Level Trigger, muon L2 candidates are required to be associated with a track reconstructed in the inner tracker with at least five hits. Isolation in the calorimeters (the sum of the tower energies in a cone of $R \leqslant 0.3$ around the track extrapolation) and in the tracker (the sum of the reconstructed track momenta in the same cone) are then determined for later use in both single-muon and dimuon triggers.

The inclusive single-muon trigger is formed by the requirement that at least one L3 muon candidate be isolated and have a momentum transverse to the beam (p_T) in excess of $14\,\text{GeV}/c$ at L1 and $19\,\text{GeV}/c$ at L3. In the dimuon trigger, a symmetric p_T threshold is set to $3\,\text{GeV}/c$ at L1 and $7\,\text{GeV}/c$ at L3. Only one of the two muons has to be isolated in that case, but both muons must originate from the same vertex (within $\pm 5\,$mm in z). Dimuons close in space and momentum ($\Delta\phi < 0.05\,$radians, $\Delta\eta < 0.01$ and $\Delta p_T < 0.1\,\text{GeV}/c$) are rejected to remove ghost muons.

The total (L1 + L2 + L3) trigger efficiency is displayed in Fig. 4a for the single-muon trigger and in Fig. 4b for the dimuon trigger, as a function of the leading and the next-to-leading muon generated muon p_T, respectively, for SUSY events generated with the LM1 parameter set. The inclusive single-muon trigger efficiency is shown for all events which contain at least one muon in the acceptance of the detector (including muons produced in heavy flavour jets). The dimuon trigger efficiency is shown only for events which contain two prompt muons originating from the SUSY cascade decay chains (excluding, for example, muons produced in heavy flavour jets).

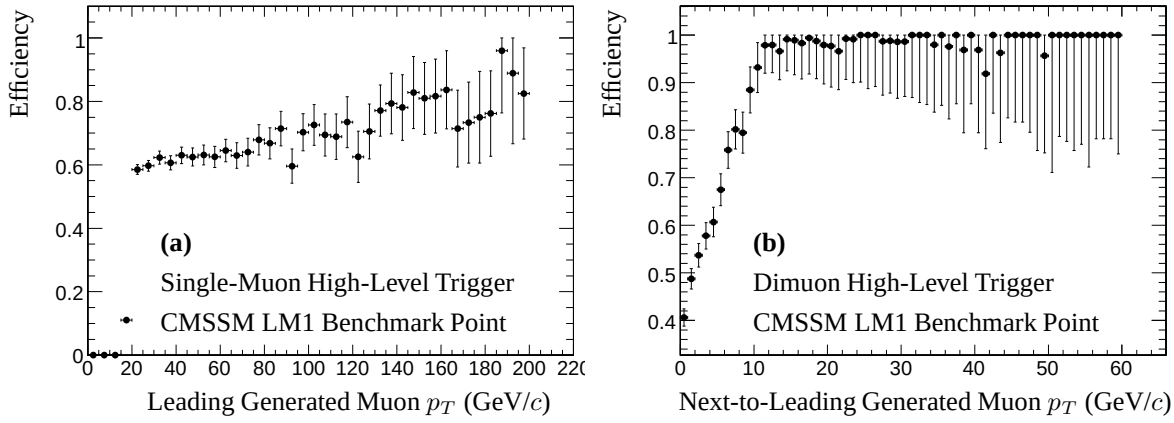

Figure 4: Left plot (a) shows inclusive single-muon HLT trigger efficiency versus the leading generated muon p_T in SUSY LM1 events. Right plot (b) shows dimuon HLT trigger efficiency as a function of the next-to-leading generated muon p_T in SUSY LM1 events which contain two prompt muons.

The single-muon analysis applies the "OR" of the single-muon trigger and the dimuon trigger, while the like-sign dimuon analysis uses solely the dimuon trigger. Table 2 shows the breakdown of the trigger efficiencies. Because not all events generated at LM1 contain a muon, the overall signal acceptance for the LM1 benchmark point

is 11.8%, but the overall trigger acceptance for events generated with a muon amounts to 29.6%. In 39.0% of these triggered events, the single-muon and dimuon events come together. Inclusively, the single-muon trigger accounts for 80.2% of the sample, whilst exclusively it accounts for 41.2%. The corresponding numbers for the dimuon trigger are 58.8% and 19.8%, respectively. Finally, 98% of the events generated with two like-sign prompt muons pass the dimuon trigger.

Table 2: Decomposition for single-muon and dimuon triggers for the CMSSM LM1 point.

Condition	Trigger	Events (%)
None	None	98 250 (100%)
At least one μ	None	38 966 (39.7%)
Inclusive	Single-μ "OR" Di-μ	11 550 (11.8%)
Inclusive	Single-μ "AND" Di-μ	4 501 (4.6%)
Inclusive	Single-μ	9 262 (9.4%)
Inclusive	Di-μ	6 789 (6.9%)
Exclusive	Single-μ	4 761 (4.8%)
Exclusive	Di-μ	2 288 (2.3%)

4.2 Physics Object Reconstruction

4.2.1 Muons

This work uses muons from the "Global Muon Reconstructor" [8] which is seeded by finding segment patterns in the CSC's or DT's. Starting with the initial segment patterns, a "forward" Kalman-filter technique is applied from the inner muon chambers to the outer muon chambers, followed by a "backward" Kalman-filter (applied from outside to inside). The track is extrapolated to the nominal interaction point and a vertex constrained fit is performed. Next, the track is extrapolated to include hits in the inner tracker. The list of final muon candidates is then made by cutting on the χ^2 of each trajectory. The selected candidates are then refitted, excluding hits with high residual values in muon stations with high occupancy.

Figure 5 shows that the efficiency to reconstruct muons as a function of both generated muon p_T and η is above 90% for p_T above 10 GeV/c and above 90% for most of $|\eta| < 2.4$ (when $p_T > 30$ GeV/c). Good agreement between ORCA and FAMOS is also observed when the same criteria are applied.

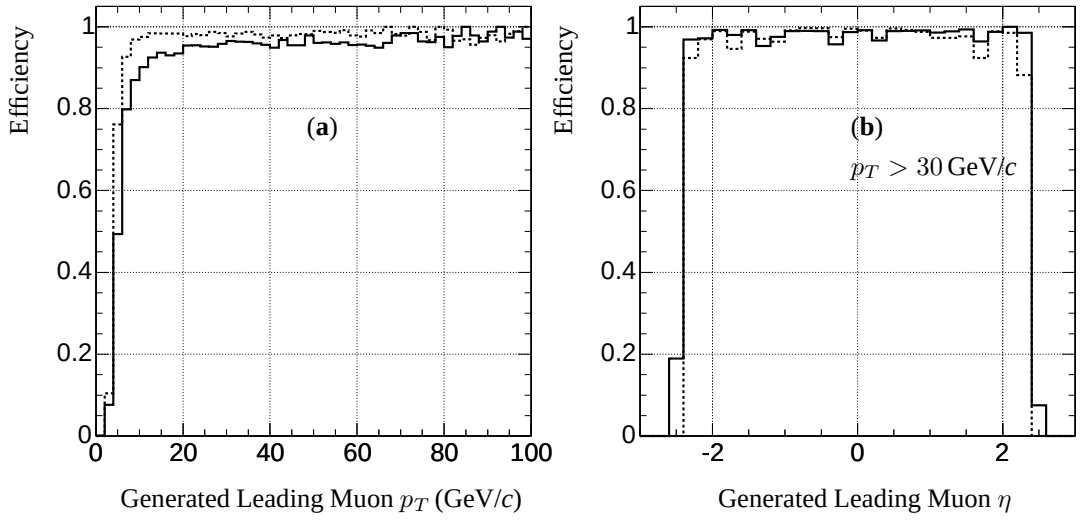

Figure 5: Global muon reconstruction effi ciencies for ORCA (solid line) and FAMOS (dotted line) versus the generated p_T (a) and η (b). The plot (b) is formed after requiring that the reconstructed muon p_T be at least 30 GeV/c.

4.2.2 Jets

Jets are reconstructed with an iterative cone algorithm [8] using the energies deposited in projective calorimeter towers. In the barrel, a calorimeter tower is formed by topologically associating a single HCAL tower to 25 (5×5) ECAL crystals. A more complex association of HCAL towers to ECAL crystals is required in the end-caps. A cone of size $R = 0.5$ in the (η,ϕ) plane is cast around the input object having the largest transverse energy above a specified seed threshold which is equal to $0.5\,\text{GeV}$. The objects inside the cone are used to calculate a "proto-jet" direction and energy using the E_T-scheme. The computed direction is used to seed a new proto-jet. The procedure is repeated until the energy of the proto-jet changes by less than 1% between iterations and the direction of the proto-jet changes by less than 0.01 in the (η,ϕ) plane. When a stable proto-jet is found, all objects in the proto-jet are removed from the list of input objects and the stable proto-jet is added to the list of jets. The whole procedure is repeated until the list contains no more objects with an E_T above the seed threshold or no jets with at least an E_T above $10\,\text{GeV}$ can be formed. Each reconstructed jet is then calibrated using average corrections from photon-jet balancing, tuned for low-luminosity pile-up.

Figure 6 demonstrates that the ORCA efficiency to reconstruct jets is above 95% for E_T above $50\,\text{GeV}$ over a broad range of η. Further, the FAMOS efficiency to reconstruct jets is very similar to that of ORCA for jet E_T above $50\,\text{GeV}$.

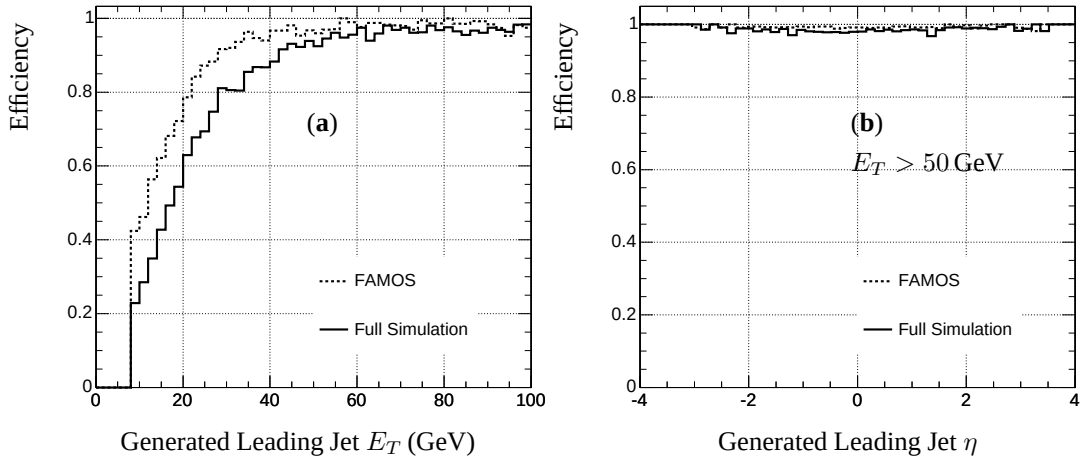

Figure 6: Jet reconstruction efficiency for ORCA (solid line) and FAMOS (dotted line) versus the generated jet E_T (a) and η (b). Plot (b) is formed after requiring that the reconstructed jet E_T be at least $50\,\text{GeV}$.

4.2.3 Missing Transverse Energy

The missing transverse energy (E_T^{miss}) is equal to absolute value of total transverse momentum ($\mathbf{p}_T$) which is calculated by summing individual calorimeter towers having energy E_n, polar angle θ_n and azimuthal angle ϕ_n [8]:

$$E_T^{\text{miss}} = |\mathbf{p}_T| = \left| -\sum_n \left(E_n \sin\theta_n \cos\phi_n \hat{\mathbf{i}} + E_n \sin\theta_n \sin\phi_n \hat{\mathbf{j}} \right) \right| \tag{1}$$

Equation 1 represents a measure of the momentum imbalance of the event from long-lived particles escaping detection in the calorimeters, such as neutrinos, muons, or the LSP.

4.3 Offline Preselection

To ensure an adequate understanding of the physics objects used in this work, quality criteria are applied to muons and jets. In the single-muon analysis, the leading muon is required to be reconstructed with a momentum in excess of $30\,\text{GeV}/c$, and both muons must be reconstructed with a p_T in excess of $10\,\text{GeV}/c$ in the dimuon analysis. These cuts ensure the muon candidates are reconstructed with good efficiency, and with a momentum well above the trigger thresholds.

In addition, muons from prompt sparticle decays are best recognized by the requirement that the χ^2 of the global trajectory fit be smaller than 3.0 per degree of freedom, and the total number of hits associated to the muon track

exceed 12. These quality cuts are $\sim 100\%$ efficient for prompt muons, but allow a fair fraction of fake muons or muons from long-lived particle ($\pi^{\pm}$, $K^{\pm}$) decays to be rejected.

Further, the leading muon (single-muon analysis) and the two leading muons (dimuon analysis) are required to be isolated with less than 10 GeV in a cone of radius 0.3 around the muon direction. In the single-muon analysis, the isolation energy is simply that measured in the calorimeter within the isolation cone, while in the dimuon analysis, it is defined as the sum of the charged particle momenta and 75% of the calorimetric energy in the isolation cone $R \leq 0.3$. These isolation requirements reject many of the muons from b- or c-quark semi-leptonic decays, not rejected by the aforementioned quality cuts, as can be seen in Fig. 7a.

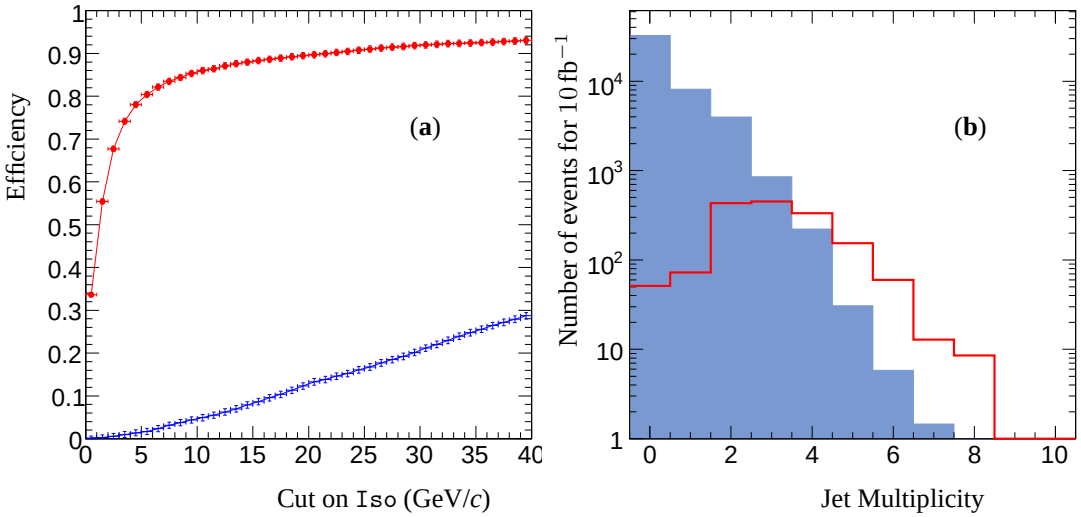

Figure 7: (a) Cut efficiencies for the general isolation parameter `Iso` for prompt reconstructed muons (top curve) and muons from hadron decays (bottom curve). (b) Jet multiplicity distributions for LM1 signal (solid line) and Standard Model backgrounds (shaded area).

Events from SUSY tend to have jet multiplicities higher than those of the Standard Model events, as seen in Fig. 7b. Both studies thus require at least 3 jets. The three leading jets must each have an E_T of at least 50 GeV which guarantees that jets are reconstructed with good efficiency (Fig. 6). No quality pre-selection requirements are made on the $E_T^{\rm miss}$, but a large $E_T^{\rm miss}$ is required during the selection optimization. Cleaning $E_T^{\rm miss}$ at the LHC, however (made necessary by non-collisional beam backgrounds, cosmic muons, electronic noise, hot/dead calorimeter channels, etc) is likely to be a challenging task and will ultimately require dedicated studies with real data. Some inspiration may be taken from the Tevatron [27]. Due to the 25 ns bunch spacing at the LHC and the large CMS detector volume, however, out-of-time effects become important in identifying non-collisional backgrounds and the applicability of the Tevatron methods can only be taken as suggestive strategies.

5 Discriminating Signal from Background

5.1 Selection Strategy and Optimization Method

Signal and background can be disentangled with a series of cuts on observables that carry some discrimination power. These observables include the three leading jet transverse energies and pseudo-rapidities, the leading and next-to-leading muon transverse momentum, the missing transverse energy, and various jet and muon isolation variables (Figs. 8, 9 and 10). The strategy is to find a set of selection cuts that optimize the significance with which the null hypothesis (only standard model backgrounds) is expected to be excluded in the presence of signal.

A genetic algorithm tool, known as GARCON [28], is used to search a multi-dimensional space of cuts, with the aim of maximizing the significance for potential discovery. Initially, the genetic algorithm randomly and coarsely samples the kinematic parameters used in the cut optimization, defining a space of particular combinations of cuts. Points in this space of cuts which result in the highest significance values are given a priority. Points, or cut sets, above a certain priority are then used to further identify other potentially interesting points in the space by either "crossing" (i.e. the exchanging of certain cuts between two cut sets) or "mutating" (i.e. the random perturbation of a certain cut value in a single cut set). This new "generation" of cut sets are then applied to the signal and background samples, and the process is repeated for a pre-defined number of generations, after which the cut set

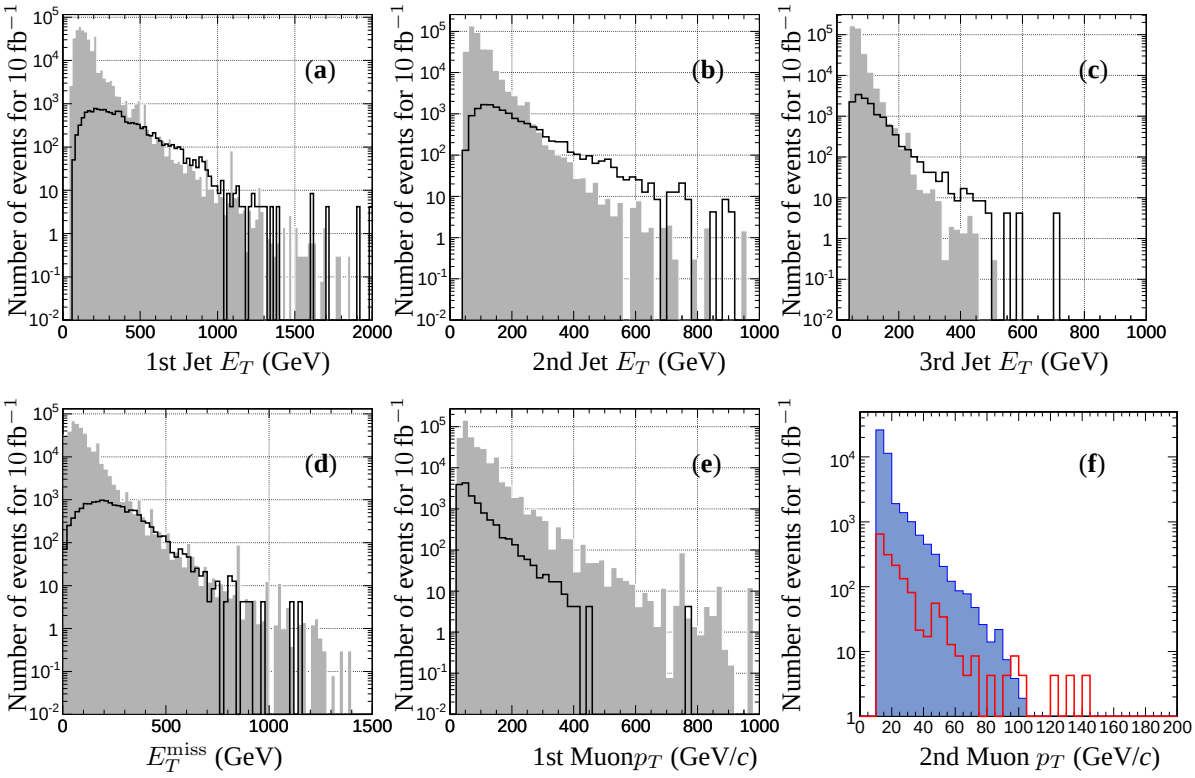

Figure 8: Distributions of variables involving transverse energies and momenta used for discriminating signal from background for the Standard Model backgrounds (shaded area) and the LM1 signal (solid black line) after the trigger and pre-selection cuts have been applied. Plots (a), (b) and (c) in first row: E_T of the three leading jets (left to right). Second row: (d) $E_T^{\rm miss}$ of the event, (e) p_T of the leading muon, and (f) p_T of the next-to-leading muon from same-sign pair. In all plots, the numbers of events are scaled to an integrated luminosity of $10\,{\rm fb}^{-1}$.

giving the maximum significance value is chosen as optimal, or until a "catastrophic event" occurs (i.e. the starting and initialization of the entire process again, to escape from a local maximum). Further details may be found in [28].

Approximations are used in the significance calculation (described separately for each analysis below) which are accurate enough for the optimization to be meaningful when the number of signal and background events are large, and simple enough for the optimization process to be manageable in terms of computing time. Once an "optimal" cut set is determined, the significance is estimated with more robust statistical methods, described in Section 6.

5.2 Selection Cuts in the Single-Muon Analysis

In the case of the single-muon analysis, the optimization is performed by explicitly including the effects of some systematic uncertainties in the significance determination, so as to avoid challenging regions of phase space. A simple estimate of the significance $S_{1\mu}$ is used in the optimization process:

$$S_{1\mu} = \frac{N_{\rm s}}{\sigma_{\rm b}} = \frac{N_{\rm s}}{\sqrt{N_{\rm b} + (\delta N_{\rm b}^1)^2 + (\delta N_{\rm b}^2)^2 + ...}}, \tag{2}$$

where $N_{\rm s}$ and $N_{\rm b}$ are the numbers of signal and background events passing all cuts, and $\delta N_{\rm b}^i$ are the systematic uncertainties on $N_{\rm b}$ due to some systematic effect i. The denominator in Eq. 2 is nothing but an estimate of the total uncertainty on the background, obtained by adding statistical and systematic uncertainties in quadrature, thereby assumed to be independent of each other. The systematic effects considered during the optimization process include, the jet energy scale (assumed to be known to within 10%), the jet energy resolution (assumed to be known to within 5%), and the uncertainty due to highly weighted simulated events.

The primary features which are exploited to separate signal from the remaining backgrounds are the distinctly harder jets and $E_T^{\rm miss}$ spectra, the centrality of the leading jets, as well as the azimuthal angles between the leading and next-to-leading jets, and between the $E_T^{\rm miss}$ vector and the leading and next-to-leading jets. Requiring central leading jets helps to distinguish heavy particles produced at rest from lighter mass particles, such as the W or Z, produced with a significant boost along the beam axis. The angular requirements are expected to be particularly effective against QCD dijets, since in such events the $E_T^{\rm miss}$ vector typically points in the direction of a mis-measured jet. Finally, as the leading muon p_T spectrum is relatively soft, when compared with the background, no additional tightening of the muon p_T cut is made when applying the final selection cuts.

A total of eleven variables (the three leading jets E_T's and η's; the difference in azimuth angles between the two leading jets as well as the $E_T^{\rm miss}$; and the leading muon p_T) is provided as input to the genetic algorithm and the results of that search, are displayed in Table 3. While the Standard Model backgrounds considered in this study have a very low efficiency ($\approx 10^{-7}\%$) to pass the final selection cuts, some background contamination into the signal region is still expected and is estimated to be 2.5 ± 0.5 Standard Model events.

5.3 Selection Cuts in the Dimuon Analysis

In the case of the dimuon analysis, the optimization is performed using the following simple likelihood ratio estimate of the significance $S_{2\mu}$:

$$S_{2\mu} \quad = \quad \sqrt{2\ln Q} = \sqrt{2(N_{\rm s} + N_{\rm b})\ln\left(1 + \frac{N_{\rm s}}{N_{\rm b}}\right) - 2N_{\rm s}}, \tag{3}$$

where Q represents the ratio of Poisson likelihoods, $N_{\rm s}$ and $N_{\rm b}$ are the numbers of signal and background events passing all cuts.

As in the inclusive single-muon case, there is a large $E_T^{\rm miss}$ excess for signal events compared with background, due to the LSP's; indeed, the $E_T^{\rm miss}$ is one of the most powerful discriminators of R-parity-conserving SUSY. The E_T spectra for the three leading jets in SUSY events tend to be significantly harder than in Standard Model events. As the muons p_T spectra are rather similar to the background, no additional tightening of the muons p_T cuts is made when applying the final selection cuts. Finally, Fig. 10 demonstrates that the leading muon, for both signal and background, already tends to be isolated and hence does not discriminate well. However, the second leading muon tends to be more isolated in the signal than in the background.

A total of nine variables (the three leading jets E_T's; the jet multiplicity; the $E_T^{\rm miss}$; the p_T and isolation of the two leading same-sign muons) are used in the genetic algorithm. Table 4 provides a summary of the numbers

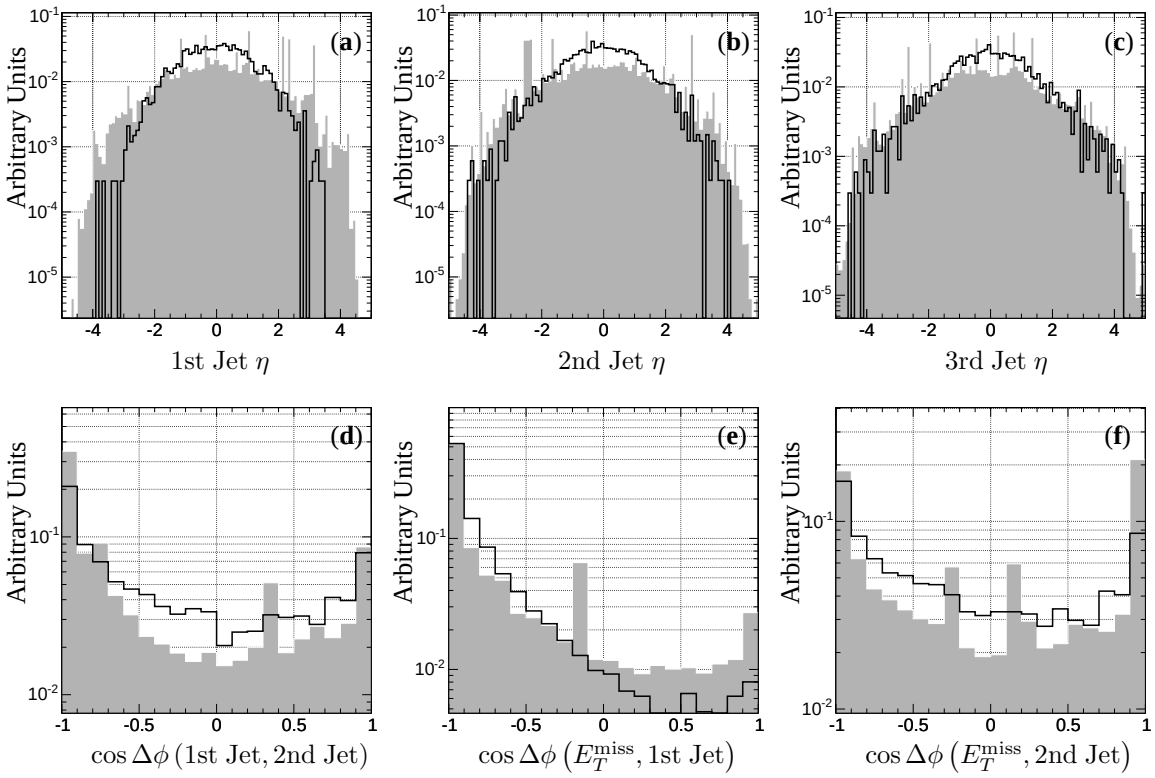

Figure 9: Distributions of variables involving angular information used for discriminating signal from background for Standard Model backgrounds (shaded area) and the LM1 signal (solid black line) after the trigger and pre-selection cuts have been applied. Plots (a), (b) and (c) in first row: η distribution of the three leading jets (left to right). Second row: cosine of the difference in azimuthal angle between (d) the leading and next-to-leading jets, (e) the $E_T^{\rm miss}$ vector and the leading jet, and (f) the $E_T^{\rm miss}$ vector and the next-to-leading jet. In all plots, the numbers of events are scaled to an integrated luminosity of $10\,\text{fb}^{-1}$. Spikes observed for the backgrounds are due to highly weighted events, and not to any particular physical feature.

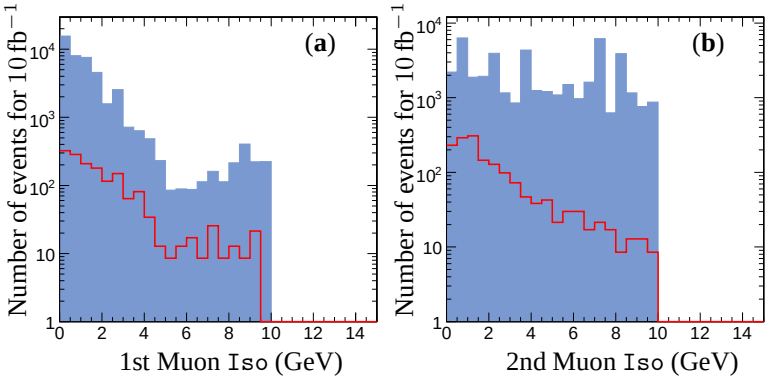

Figure 10: Distributions of the two leading muon isolation variables for the Standard Model background (shaded area) and the LM1 signal (solid black line) after the pre-selection cuts have been applied. Left plot (a) shows isolation parameter of leading muon in the same sign pair. Right plot (b) shows isolation parameter of next-to-leading muon in the same sign pair. In both plots, the numbers of events are scaled to an integrated luminosity of $10\,\text{fb}^{-1}$.

Table 3: All selection cuts as applied in the inclusive single-muon analysis. First category: event topology and quality pre-selection cuts. Second category: signal selection cuts determined by the genetic algorithm. Third category: trigger requirements. While some selection cuts appear to only marginally discriminate the signal from backgrounds, they nevertheless improve the overall significance (as defined by Eq. 2) by reducing systematic uncertainties.

	Cut Criteria			LM1	SM
Pre-selection	number of muons ≥ 1 "AND" p_T	$>$	30 GeV/c	45450 (10%)	7.383×10^7 (10^{-5}%)
	μ calo. iso. ($R = 0.3$) E_T	$<$	10 GeV	24260 (53%)	5.26×10^7 (71%)
	number of jets ≥ 3 "AND" E_T	$>$	50 GeV	15660 (64%)	3.769×10^4 (0.07%)
Selection	leading jet (Jet1) E_T^{Jet1}	$>$	440 GeV	4062.0 (25%)	3271.0 (1%)
	next-to-leading jet (Jet2) E_T^{Jet2}	$>$	440 GeV	656.0 (16%)	536.1 (16%)
	$\lvert\eta^{\mathrm{Jet1}}\rvert$	$<$	1.9	639.2 (97%)	500.9 (93%)
	$\lvert\eta^{\mathrm{Jet2}}\rvert$	$<$	1.5	567.7 (88%)	445.9 (89%)
	$\lvert\eta^{\mathrm{Jet3}}\rvert$	$<$	3.0	559.3 (98%)	313.4 (70%)
	$-1 < \cos\left[\Delta\phi(\mathrm{Jet1},\ \mathrm{Jet2})\right]$	$<$	0.2	525.6 (93%)	311.3 (99%)
	$-0.95 < \cos\left[\Delta\phi(E_T^{\mathrm{miss}},\ \mathrm{Jet1})\right]$	$<$	0.3	407.9 (77%)	81.4 (26%)
	$-1 < \cos\left[\Delta\phi(E_T^{\mathrm{miss}},\ \mathrm{Jet2})\right]$	$<$	0.85	386.9 (94%)	34.0 (42%)
	E_T^{miss}	$>$	130 GeV	328.0 (84%)	3.7 (11%)
Trigger	single-μ "OR" di-μ	$=$	"Accept"	311.2 (94%)	2.5 (69%)

of selected events, after sequentially applying the cuts for both signal and background. The effect of the trigger, quality pre-selection cuts, and the SUSY diagram selection cuts (but without muon isolation) strongly suppresses all backgrounds. Next, the optimized muon isolation cuts on both muons are applied which dramatically suppresses the QCD background. The effect of requiring three jets in the event allows for a significant reduction in the number of WW + jets background. Following that, cuts on the transverse energy of jets are applied. Finally, the cut on missing transverse energy reduces all remaining Standard Model backgrounds by two orders of magnitude. The total number of remaining Standard Model background events is estimated to be 1.5 ± 0.3 and comes solely from $\mathrm{t\bar{t}}$ production. The muon isolation requirements are also a key factor in selecting events corresponding to SUSY diagrams with prompt muons. Indeed, the dimuon analysis selects such diagrams with $\sim 65\%$ efficiency and over $\sim 90\%$ purity. The impact of statistic and systematic uncertainties is described in the following section.

Table 4: All selection cuts as applied in the dimuon analysis. First category: cuts which distinguish SUSY diagrams involving prompt same-sign dimuons together with quality pre-selection criteria. Second category: signal selection cuts determined by the genetic algorithm. Third category: trigger requirement.

	Cut Criteria			LM1	SM
Pre-selection	2 same-sign muons with p_T	$>$	10 GeV/c	4813 (1.1%)	8×10^7 (10^{-5}%)
	number of hits per μ track ≥ 13 and χ^2_μ	$<$	3	4191 (87%)	2×10^6 (2.5%)
	isolation $\mathtt{Iso}_{\mu 1} < 10$ GeV and $\mathtt{Iso}_{\mu 2}$	$<$	6 GeV	1481 (35%)	29368 (1.5%)
	number of jets ≥ 3 with E_T	$>$	50 GeV	947 (64%)	636 (2.2%)
Selection	next-to-next-to-leading jet E_T^{Jet3}	$>$	55 GeV	883 (93%)	477 (75%)
	next-to-leading jet E_T^{Jet2}	$>$	130 GeV	555 (63%)	38 (8%)
	leading jet E_T^{Jet1}	$>$	175 GeV	529 (95%)	28 (74%)
	E_T^{miss}	$>$	200 GeV	341 (64%)	1.5 (5%)
Trigger	di-μ HLT	=	"Accept"	341 (100%)	1.5 (100%)

6 Systematic Cross-checks and Uncertainties

6.1 Limited Amount of Simulated Data

Because the different simulated samples used in this study were each produced with different integrated luminosities, the acceptance of each sample is determined after each sample has been scaled to an equivalent integrated luminosity of 10 fb^{-1}. The luminosity-weighted number of events N_w (for a given dataset) which pass each cut is given by $N_w = wN_{\mathtt{Gen}}$ where $w = (10\ \mathrm{fb}^{-1})/L_{\mathtt{Gen}}$ and where $N_{\mathtt{Gen}}$ is the un-weighted number of events that pass each cut, assuming an integrated luminosity for the generated sample of $L_{\mathtt{Gen}}$. Hence, simulated data pro-

duced with a limited number of events, much less than the assumed $10\,\text{fb}^{-1}$ of data, lead to highly weighted event samples and hence large uncertainties on the predicted background level.

In the inclusive single-muon analysis, the total statistical uncertainty due to the limited number of events simulated is determined to be $\sim$32%. In the dimuon analysis, after all cuts have been applied, no multi-jet QCD events are selected. As a cross-check, the statistical uncertainty on the number of multi-jet events, which are expected to pass the selection cuts, may be estimated by factorizing the full n-dimensional cut set into n independent subsamples corresponding to a single cut. Also, because the summed p_T of the event (known as H_T) strongly correlates with $\hat{p}_T$ ($H_T \approx 2\hat{p}_T$), it can be used to effectively limit the amount of contamination from low $\hat{p}_T$ QCD dijet events. In this work, the final cuts on transverse energy of jets and missing energy (Section 5.3) imply that $H_T = \sum_{\text{Jets}} E_T^{\text{Jet}} + E_T^{\text{miss}} \approx 560\,\text{GeV}$.

Conservatively considering all QCD dijet samples with $\hat{p}_T > 120\,\text{GeV}/c$ (since $H_T > 560\,\text{GeV}$ in this work) and by applying each cut individually, (1) the probability that a QCD dijet event passes the selection requirements for two same-sign muons with transverse momentum $p_T^{\mu} > 10\,\text{GeV}/c$ is $Pr(\mu^{\pm}\mu^{\pm}) \approx (1.2 \pm 0.1) \times 10^{-4}$, (2) the probability for any muon from a QCD dijet event to be isolated is $Pr(\mathsf{Iso}) \approx (3.2 \pm 0.2) \times 10^{-2}$ and finally (3) the probability that a QCD dijet event passes the requirement on missing transverse energy $E_T^{\text{miss}} > 200\,\text{GeV}$ is equal to $Pr(E_T^{\text{miss}}) \approx (1.1 \pm 0.1) \times 10^{-4}$. Hence, the probability that a QCD dijet event passes all selection requirements is estimated by:

$$P = P(\mu^{\pm}\mu^{\pm}) \times Pr(\mathsf{Iso}) \times Pr(\mathsf{Iso}) \times Pr(E_T^{\text{miss}}) \approx (1.8 \pm 0.3) \times 10^{-11}. \tag{4}$$

Small correlations between different cuts are not taken into account. For instance, Pearson's correlation coefficient between cuts (1) and (3) is approximately equal to 0.2. Since the number of QCD dijet events (Table 9) from all samples with $\hat{p}_T > 120\,\text{GeV}/c$ (for an integrated luminosity of $10\,\text{fb}^{-1}$) is $N_{\text{jj}} \approx 6.34 \times 10^9$, the estimated upper limit on the number of QCD dijet events which pass all cuts is $N_{\text{jj}} \lesssim 0.1 \pm 0.02$. Hence the statistical uncertainty is small, despite the huge weights applied to low $\hat{p}_T$ samples.

By the time $10\,\text{fb}^{-1}$ of data has been collected, many of the Standard Model backgrounds such as electro-weak processes will however be directly measured at the LHC (using, for example, the method outlined in Ref. [29]). This uncertainty represents today's ignorance but is expected to be mitigated somewhat by the time $10\,\text{fb}^{-1}$ of data is collected. Moreover, in the future, it is expected that additional simulated data will be produced, which may be nearly sufficient for $\hat{p}_T$ greater than the effective value of $280\,\text{GeV}/c$ required in this work. Hence, the estimated effect of the limited amount of simulated data used in this work is presented as a cross-check and is not applied as a systematic uncertainty.

6.2 Jet Energy Scale

These analyses use the transverse energy of the three leading jets as well as the missing transverse energy of the event as variables which discriminate between the SUSY signal and the Standard Model backgrounds. Because the number of background events falls steeply when increasing the E_T^{miss} cut, but the fraction of signal events which pass the cut decreases slowly, even small uncertainties in the jet energy and missing transverse energy scale can lead to large uncertainties in the background acceptance and the corresponding estimated significance for possible discovery. By the time $10\,\text{fb}^{-1}$ of integrated luminosity is gathered, the CMS Jet Energy Scale (JES) is expected to be calibrated at the level of 3% via a W mass constraint in semi-leptonic $\text{t}\bar{\text{t}}$ events. Accordingly, a scaling is applied to all reconstructed jet E_T's and the E_T^{miss} by $\pm$3%. A 100% correlation between the reconstructed jet E_T's and the reconstructed E_T^{miss} is assumed.

The number of events which pass the altered case is compared with the number of events which pass the unaltered case and the corresponding systematic uncertainty, due to jet energy scale, is then taken as the difference between the two cases,

$$\delta N_{\text{b}}^{\text{JES}\ \pm 3\%} \approx N_{\text{b}}^{\text{JES}\ \pm 3\%} - N_{\text{b}}. \tag{5}$$

6.3 Jet Energy Resolution

Similar to the Jet Energy Scale, uncertainties in the Jet Energy Resolution can lead to systematic uncertainties in the estimated significance. With $10\,\text{fb}^{-1}$ of integrated luminosity, the resolution of CMS jet energies are expected to be known to within 10% via dijet balancing. Accordingly, a Gaussian smearing is applied to all reconstructed jet transverse energies, according to the formula below. The missing transverse momentum $\mathbf{p}_T^{\text{miss}}$ (whose magnitude

is simply $E_T^{\rm miss}$) is assumed to be 100% correlated with the jets, and $\mathbf{p}_T^{\rm miss}$ is correspondingly modified, event by event, according to the smeared jet energy:

$$E_T^{{\rm Jet}i} \rightarrow E_T^{{\rm Jet}i} + 0.1 \ \texttt{Gaussian}[1,0] \ E_T^{{\rm Jet}i}, \quad (6)$$

$$\mathbf{p}_T^{\rm miss} \rightarrow \mathbf{p}_T^{\rm miss} - \sum_i \Delta \mathbf{p}_T^{{\rm Jet}i}, \quad (7)$$

assuming massless jets $E_T^{\rm Jet} = |\mathbf{p}_T^{\rm Jet}|$ and where $E_T^{\rm miss} = |\mathbf{p}_T^{\rm miss}|$. The number of events which pass in the altered case is compared with the number of events which pass in the unaltered cases and the systematic uncertainty, due to jet energy resolution, is then taken as the difference between the two cases:

$$\delta N_{\rm b}^{\rm JER\ \pm 10\%} \approx N_{\rm b}^{\rm JER\ \pm 10\%} - N_{\rm b}. \quad (8)$$

6.4 Muon Identification Efficiency and Fake Rate

The systematic uncertainty in the muon p_T, due to uncertainties in the magnetic field, is $\delta p_T = 0.5\% p_T$ and translates to a negligible uncertainty in the efficiency to trigger and reconstruct muons in these analyses.

The probability of fake muons which pass the calorimeter isolation cut and so contribute to this analysis is less than 0.03% in the single-muon analysis and less than 1% in the dimuon analysis. The fake rate is larger in the latter because each of the two muons may be fake, and because the leading muon momentum cut is looser. The systematic uncertainty on the fake muon rate is assumed, *ad hoc*, to be 10% of the probability observed in the simulation, which leads to a negligible uncertainty on the rate of backgrounds passing the selection cuts due to fake muons.

6.5 Effect of Fake $E_T^{\rm miss}$ due to Beam Halo Background

The amount of beam halo which may affect physics event data arises primarily from either (1) a beam halo particle arriving in coincidence with an event triggered solely due an actual hard scattered process or (2) a beam halo particle promoting a min-bias event, which would not have normally triggered the event. Since this work uses only the single-muon and dimuon triggers, the second scenario is neglected. A beam-halo particle would not lead to additional identified muons, but may affect the jets and missing energy triggers. The rate of beam-halo events with $E_T^{\rm miss}$ above $25\,$GeV is estimated to be $1250\,$Hz and corresponds to a probability of 3×10^{-5} that any given ($25\,$ns) bunch crossing contains such a beam halo particle. Since these analyses use the muon triggers, the probability that any given bunch crossing contains a single-muon or dimuon triggered event *together* with a beam halo event is approximately 2×10^{-11}. By integrating over all bunch crossings up to $10\,{\rm fb}^{-1}$ of data and applying all selection cuts, except those involving $E_T^{\rm miss}$, the total number of background events expected to contain a superimposed beam halo particle is estimated to be 2×10^{-3}, or much less than one event. Hence, the systematic uncertainty associated with a superimposed beam-halo particle, which could promote a background event originally having $E_T^{\rm miss} < 105\,$GeV beyond the selection cut of $E_T^{\rm miss} > 130\,$GeV, is negligible.

6.6 Theory

As already mentioned, the acceptance of high E_T ISR/FSR jets as generated by PYTHIA can be significantly underestimated in these studies. Since the two leading jets in both the inclusive single-muon and the dimuon analyses are required to be very hard, the difference in the modelling of ISR/FSR is assumed to primarily affect the efficiency of the E_T cut on the third leading jet. The effect on the efficiency to select the third jet is then estimated by comparing inclusive $\rm t\bar{t}$ events simulated with a parton shower method from PYTHIA with $\rm t\bar{t}+1$ jet events simulated using a full matrix element calculation from CompHEP [30]. The full matrix element calculation increases the relative acceptance of $\rm t\bar{t}+1$ jet events by approximately 10%, which is taken as a systematic uncertainty due to ISR/FSR.

In addition to ISR/FSR, other theoretical effects involving (1) pile-up, (2) underlying event and (3) parton distribution function (PDF) uncertainties are each assumed to be at the level of 5%. Hence, assuming all effects to be uncorrelated, a total systematic uncertainty of 13% is estimated due to theoretical uncertainties. Further studies (beyond the scope of this work) will be required to more precisely estimate the systematic uncertainties due to theoretical concerns. The rough estimate of 13% theoretical uncertainty for this work primarily reflects the expectation that by the time CMS has collected $10\,{\rm fb}^{-1}$ of data, the QCD scale should be known to next-to-leading order and PDF uncertainties should to be understood at a similar level as at the Tevatron, where uncertainties are also typically 5-10%.

6.7 Luminosity

Reference [8] indicates that once approximately $10\,\mathrm{fb}^{-1}$ of integrated luminosity has been collected by CMS, the uncertainty in measuring that integrated luminosity is estimated to be $\sim 5\%$. Accordingly, a 5% smearing effect in the final significance calculation is included.

6.8 Differences Between the Full and Fast Simulation and Reconstruction

Because the fast and the full simulations may not agree perfectly for all aspects of the various distributions used by this work, the signal selection efficiencies determined for a series of benchmark points (LM1, LM4, LM5, LM6, and HM1) with both simulations are compared. This comparison is displayed in Table 5, which shows that the average relative difference between full and fast simulted efficiencies is found to be $(5.4 \pm 2.2)\%$. This difference does not appear to systematically depend on the benchmark point chosen, within the statistical accuracy of the test. All FAMOS efficiencies were therefore reduced by 5.4% and a systematic uncertainty of 2.2% assigned to this number.

Table 5: Effi ciencies to selection different validation/benchmark CMSSM points between FAMOS and OSCAR/ORCA. The average relative difference in effi ciency between the fast and the full simulation/reconstruction is $(5.4 \pm 2.2)\%$.

	$\epsilon^{\mathtt{sel}}_{\mathtt{FAMOS}}$	$\epsilon^{\mathtt{sel}}_{\mathtt{ORCA}}$	$\epsilon^{\mathtt{sel}}_{\mathtt{ORCA}}/\epsilon^{\mathtt{sel}}_{\mathtt{FAMOS}}$
LM1	$(0.078 \pm 0.009)\%$	$(0.078 \pm 0.009)\%$	$(100.2 \pm 16.0)\%$
LM4	$(0.150 \pm 0.012)\%$	$(0.147 \pm 0.012)\%$	$(97.6 \pm 11.6)\%$
LM5	$(0.304 \pm 0.018)\%$	$(0.307 \pm 0.017)\%$	$(100.8 \pm 8.1)\%$
LM6	$(0.721 \pm 0.028)\%$	$(0.775 \pm 0.027)\%$	$(107.4 \pm 5.2)\%$
HM1	$(3.02 \pm 0.05)\%$	$(2.72 \pm 0.05)\%$	$(90.1 \pm 2.6)\%$
Average	–	–	$(94.6 \pm 2.2)\%$

6.9 Estimator used for Significance Calculation

Table 6 shows the final list of all systematic uncertainties considered in this analysis.

Table 6: List of systematic uncertainties considered in this work.

Systematic	Uncertainty ($\delta N/N$)	
	single-muon	dimuon
Jet Energy Scale	10%	15%
Jet Energy Resolution	5%	10%
Luminosity	5%	5%
Theory	13%	13%
ORCA vs FAMOS	2%	2%
Background Total	18%	23%

The above systematic uncertainties are incorporated in the following way. The Poisson probability to observe N events, assuming a hypothesis of number of Standard Model background events N_{b} is,

$$p(N|N_{\mathrm{b}}) = \frac{N_{\mathrm{b}}^{N}}{N!}\exp[-N_{\mathrm{b}}]. \tag{9}$$

The number of predicted background events N_{b} may be factor k different from the unknown "true" background n_{b}, due to some systematic uncertainty. Because the prediction for N_{b} is often close to zero, the number of "true" background events n_{b} is assumed to have a log-normal distribution about the prediction N_{b}:

$$f(n_{\mathrm{b}}|N_{\mathrm{b}}) = \frac{1}{\sqrt{2\pi}\,\ln k}\exp\Big[-\frac{1}{2}\Big(\frac{\ln n_{\mathrm{b}} - \ln N_{\mathrm{b}}}{\ln k}\Big)^{2}\Big]. \tag{10}$$

Hence, for a total number of background events N_{b}, predicted with a systematic uncertainty included as in Eq. 10,

the probability density to observe N events is

$$\phi(N|N_{\rm b}) = \int_0^\infty p(N|n_{\rm b}) f(n_{\rm b}|N_{\rm b}) dn_{\rm b}. \tag{11}$$

The incompatibility of the signal plus background ($N_{\rm s} + N_{\rm b}$) with the background-only hypothesis ($N_{\rm b}$) is then estimated by converting the one-sided probability tail:

$$P(N_{\rm s}, N_{\rm b}) = \int_{N_{\rm s}+N_{\rm b}}^\infty \phi(N|N_{\rm b}) dN, \tag{12}$$

to a Gaussian-equivalent significance S, by solving the equation:

$$\frac{1}{2} - \int_0^S \frac{1}{\sqrt{2\pi}} e^{-\frac{x^2}{2}} dx = P(N_{\rm s}, N_{\rm b}). \tag{13}$$

Because the probability $P(N_{\rm s}, N_{\rm b})$ is calculated via numerical integration before being converted to a significance, the estimation for S is limited by the numerical precision of the computation. As a result, estimates for S are found to be numerically robust for values up to 37σ.

7 Results

7.1 Reach for integrated luminosity of 10 fb^{-1}

The main results of these studies are shown in Table 7. For the different fully simulated low mass CMSSM points (excluding LM10) and integrated luminosity $10\,\text{fb}^{-1}$ of data, the selection cuts achieve a separation of signal from background with a statistical significance from 23σ to 34σ in the inclusive single-muon analysis and 16σ to greater than 37σ in the dimuon analysis, including systematic uncertainties. Such large values of significance merely indicate that the low mass CMSSM region will either have been discovered or excluded, long before $10\,\text{fb}^{-1}$ of data is collected. Shortly after the LHC start-up, the systematic understanding of the CMS detector is expected to be quite different than what is presented in this work, which assumes integrated luminosity of $10\,\text{fb}^{-1}$. Nevertheless, assuming a similar systematic understanding and extrapolating the results of this work to early running, the expected luminosity required to discover the LM1 study point would be order of $0.1\,\text{fb}^{-1}$ and strongly suggest (provided systematic uncertainties can be brought under control) that most of the low mass CMSSM points are well within reach of CMS during the early running of the LHC.

The significance for possible discovery of high mass SUSY, represented by the fully simulated HM1 point, with $10\,\text{fb}^{-1}$ of data appears to be challenging, but possible, in the inclusive single-muon analysis with a potential of 5σ, given $10\,\text{fb}^{-1}$ of data.

Figure 11 shows the 5σ reach contours for both analyses (including systematic uncertainties) in the CMSSM $(m_0, m_{1/2})$ plane, assuming integrated luminosity of $10\,\text{fb}^{-1}$. A comparison of the inclusive single-muon reach contours of Fig. 11 with the gluino and squark iso-mass contours given in Fig. 12 shows that CMS can observe SUSY mass scales of over $\sim 1.5\,\text{TeV}/c^2$ given $10\,\text{fb}^{-1}$ of data. Because of the high purity in which the dimuon analysis selects SUSY diagrams involving prompt same-sign muons, interesting features in the reach contours are observed. The dip in significance near $m_{1/2} = 500$ GeV/c^2, $m_0 = 500$ GeV/c^2 corresponds to tau-enriched final states (and hence a corresponding deficit of muon final states) and the bump near $m_{1/2} = 600$ GeV/c^2, $m_0 = 1100$ GeV/c^2 suggests a transition from squark-squark dominated production to gluino-gluino dominated production.

7.2 Reach beyond integrated luminosity of 10 fb^{-1}

As argued in the above section, CMS will have either discovered or excluded the lower mass region well in advance of the time required to collect $10\,\text{fb}^{-1}$ of data. Therefore, the inclusive single-muon analysis re-optimizes the cuts to select the HM1 point assuming integrated luminosity of $100\,\text{fb}^{-1}$ (to facilitate a comparison with Ref. [31]). The corresponding cut values are listed in Table 8 and result in an estimated Standard Model background yield of $N_{\rm b} = 0.25$ for $30\,\text{fb}^{-1}$ and $N_{\rm b} = 0.49$ for $60\,\text{fb}^{-1}$. Assuming $30\,\text{fb}^{-1}$ of integrated luminosity, several of the high mass CMS SUSY benchmark points become interesting for possible discovery (Fig. 11). Assuming $60\,\text{fb}^{-1}$ of integrated luminosity and comparing Figs. 11 and 12, CMS is able to reach SUSY mass scales of up to $\sim 2\,\text{TeV}/c^2$.

In the case of the dimuon analysis, no re-optimization of the selection cuts is performed for higher luminosity.

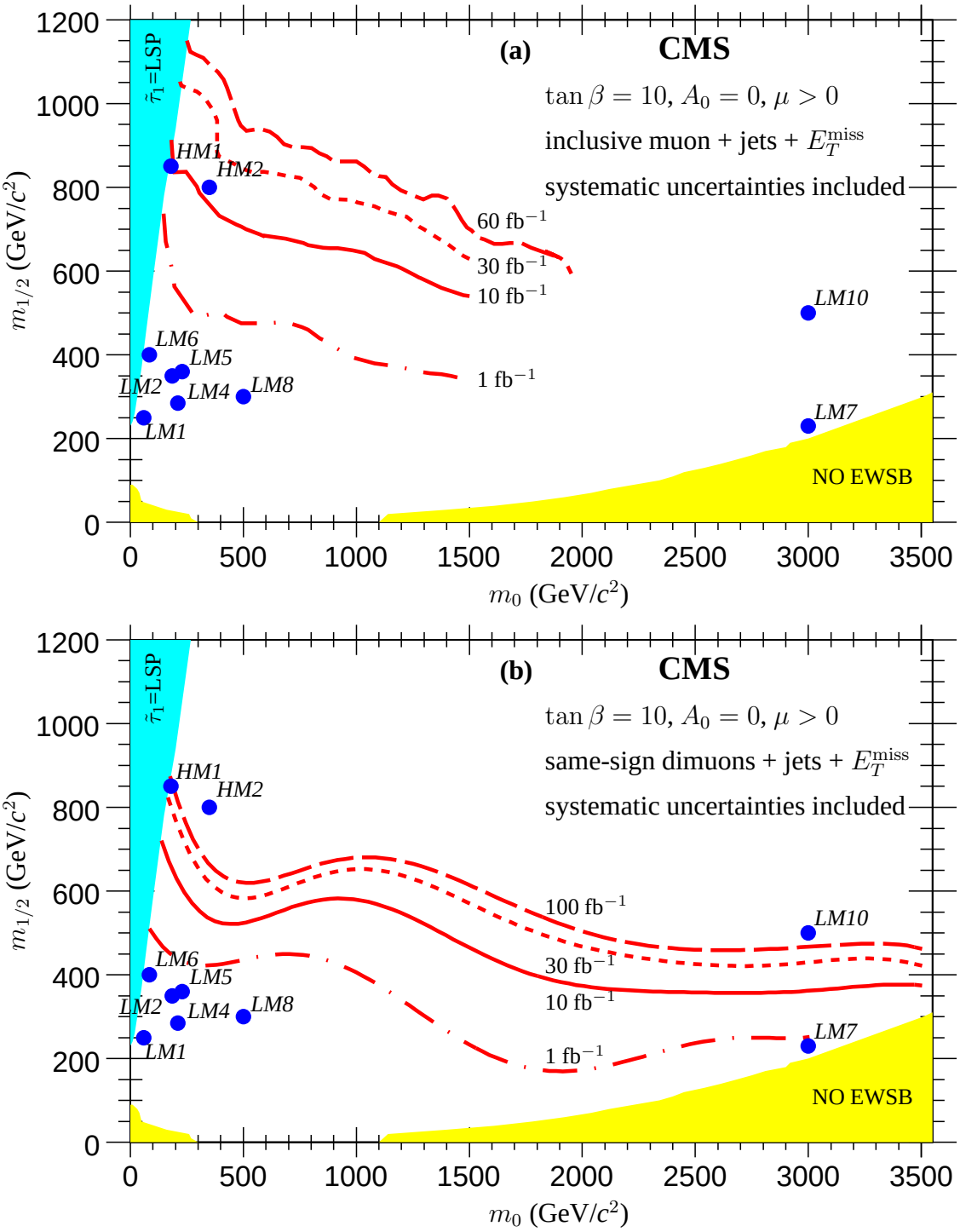

Figure 11: The top plot (a) displays the inclusive single-muon 5σ CMS reach contours in the $(m_0, m_{1/2})$ plane for integrated luminosity of 1 fb^{-1} (dot-dashed line), 10 fb^{-1} (solid line), 30 fb^{-1} (dotted line) and 60 fb^{-1} (dashed line) including systematic uncertainties; the reach curves for 1 fb^{-1} and 10 fb^{-1} are optimized to select the point LM1; the reach curves for 30 fb^{-1} and 60 fb^{-1} are optimized to select the point HM1. The lower plot (b) displays the dimuon 5σ CMS reach contours in the $(m_0, m_{1/2})$ plane for integrated luminosity of 1 fb^{-1} (dot-dashed line), 10 fb^{-1} (solid line), 30 fb^{-1} (dotted line) and 100 fb^{-1} (dashed line) including systematic uncertainties, collectively optimized to select all benchmark points. Both reach contour plots assume fi xed CMSSM parameters of: $\tan\beta = 10$, $A_0 = 0$ and $\mu > 0$.

Table 7: Total numbers of background and signal events which pass the optimized selection cuts for $10\,\mathrm{fb}^{-1}$, together with the corresponding signifi cance S (with and without systematic uncertainties) to discover the different signal benchmark points. The signifi cance is calculated according to the method described in Section 6.9

.

	single-muon analysis			dimuon analysis		
	Events ($10\,\mathrm{fb}^{-1}$)	S w/o syst.	S w/ syst	Events ($10\,\mathrm{fb}^{-1}$)	S w/o syst.	S w/ syst.
QCD	0	–	–	0	–	–
$\mathrm{t\bar{t}}$	0.7	–	–	1.5	–	–
W + jets	1.6	–	–	0	–	–
Z + jets	0.3	–	–	0	–	–
WW + jets	0	–	–	0	–	–
WZ + jets	0	–	–	0	–	–
ZZ + jets	0	–	–	0	–	–
Total	2.5	–	–	1.5	–	–
ORCA LM1	311	> 37.0	34.1	341	> 37.0	> 37.0
ORCA LM2	–	–	–	94	24.4	17.9
ORCA LM4	246	> 37.0	29.4	90	23.8	17.4
ORCA LM5	165	32.5	23.0	61	18.5	14.3
ORCA LM6	277	> 37.0	31.7	140	31.4	22.5
ORCA LM7	–	–	–	82	22.4	16.6
ORCA LM8	–	–	–	294	> 37.0	36.1
ORCA LM10	–	–	–	4	2.4	2.2
ORCA HM1	13	5.4	5.0	4	2.4	2.2
ORCA HM2	–	–	–	2	1.2	1.1
FAMOS LM1	278	> 37.0	31.7	339	> 37.0	> 37.0
FAMOS LM4	243	> 37.0	29.1	89	22.9	16.9
FAMOS LM5	156	31.3	22.2	60	17.7	13.9
FAMOS LM6	–	–	–	141	30.5	21.9
FAMOS LM7	–	–	–	81	21.5	16.1
FAMOS LM10	–	–	–	4	2.4	2.2
FAMOS HM1	13	5.4	5.0	4	2.4	2.2

8 Conclusion

This work demonstrates that the low mass CMSSM benchmark point LM1 will be easily observable given $10\,\mathrm{fb}^{-1}$ of data. The optimized cuts are used to scan across $(m_0, m_{1/2})$ plane, and the results indicate that most of the low mass region for $\tan\beta = 10$, $A_0 = 0$ and $\mu > 0$ can be observed up to mass scales of $\sim 1.5\,\mathrm{TeV}/c^2$, including systematic effects. With $30\,\mathrm{fb}^{-1}$ of data, the high mass SUSY benchmark points become interesting for possible discovery and with $60\,\mathrm{fb}^{-1}$ of data, SUSY mass scales beyond $2\,\mathrm{TeV}/c^2$ can be probed, including systematic uncertainties.

Finally, it is interesting to comment on the future direction that the dimuon work will take. The gluino, being a Majorana particle, has equal probability of yielding either a positively or a negatively charged muon in its decay chain. Therefore, dimuon events due to gluino pair production will have like-sign muons 50% of the time and there is no asymmetry between the number of two same-sign anti-muons versus the number of two same-sign muons. However, squark production is also an important source of like-sign dimuons, since the squark charge tends to be determined by the valence quarks in the proton-proton collision. Since at high x (where x is the fraction of the proton momentum carried by the hard-scattered parton) the valence composition of the proton dominates, a $4{:}1$ asymmetry is expected in the number of two same-sign anti-muons versus the number of two same-sign muons. Hence, comparing the production rate of two same-sign anti-muons with the number of two same-sign muons, squark-squark production may be distinguished from gluino-gluino production.

Acknowledgments

The authors of this work would like to graciously acknowledge the very useful and interesting discussions with Chris Tully, Jim Rohlf, Maria Spiropulu, Luc Pape, and Salavat Abdullin. In addition, this work would not have

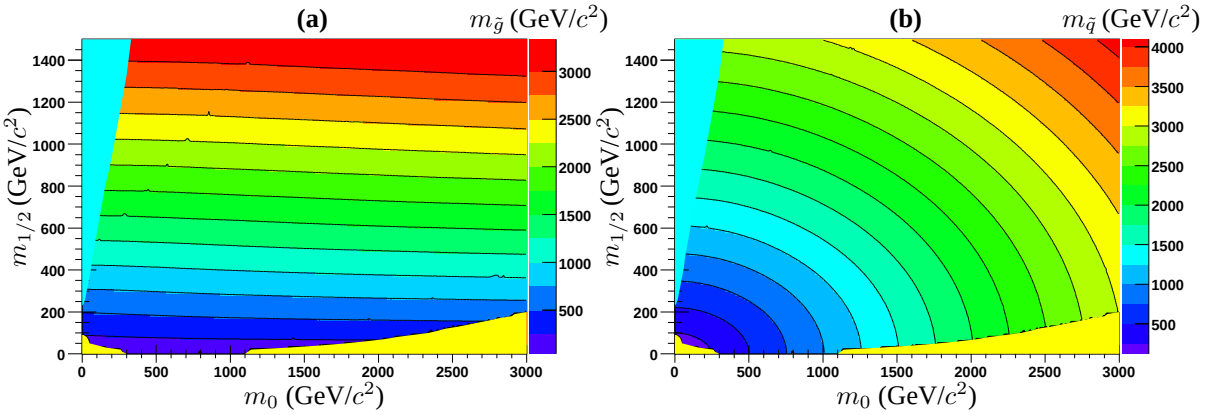

Figure 12: The left plot (a) displays the iso-mass contours for different gluino masses $m_{\tilde{g}}$ as a function of m_0 and $m_{1/2}$. The right plot (b) displays the iso-mass contours for different squark masses $m_{\tilde{q}}$ as a function of m_0 and $m_{1/2}$. Both plots assume fixed CMSSM parameters of: $\tan\beta = 10$, $A_0 = 0$ and $\mu > 0$.

Table 8: Cuts for the inclusive single-muon analysis which are re-optimized to select the HM1 benchmark point, as determined by the genetic algorithm for integrated luminosity of 100 fb^{-1}. The standard trigger and quality pre-selection cuts described in the text are implicit.

Cut Criteria		
E_T^{miss}	$>$	210 GeV
leading jet (Jet1) E_T	$>$	730 GeV
next-to-leading jet (Jet2) E_T	$>$	730 GeV
$\cos\left[\Delta\phi(\text{Jet1, Jet2})\right]$	$<$	0.95
$\cos\left[\Delta\phi(E_T^{\text{miss}}, \text{Jet1})\right]$	$<$	-0.19
$\cos\left[\Delta\phi(E_T^{\text{miss}}, \text{Jet2})\right]$	$<$	0.95

been possible without the excellent support from Craig Prescott, Jorge Rodriguez, Yu Fu at the University of Florida CMS Tier-2 Centre and Ian Fisk, Lisa Giacchetti, Joseph Kaiser, Hans Wenzel, Avi Yagil and other people at the FermiLab CMS Tier-1 Centre. The authors also gratefully acknowledge their extensive use of computing resources from the LHC Computing Grid and the Open Science Grid, which were critical to the success of this study. Finally, the authors wish to thank the two CMS referees for this Note, Wolfgang Adam and Patrick Janot, for their many useful suggestions which ultimately improved this work significantly.

A Background Datasets

Table 9: Fully simulated QCD dijet and $\mathrm{t\bar{t}}$ background samples used in this work.

Process	Bin	$\hat{p}_T$ range (GeV/c)	$\sigma_{\mathtt{LO}}$ (pb)	N (10^3 events)	L (fb^{-1})
QCD	1	$0 < \hat{p}_T < 15$	5.5×10^{10}	23	4.2×10^{-10}
QCD	2	$15 < \hat{p}_T < 20$	1.5×10^{9}	44	2.9×10^{-8}
QCD	3	$20 < \hat{p}_T < 30$	6.4×10^{8}	89	1.4×10^{-7}
QCD	4	$30 < \hat{p}_T < 50$	1.6×10^{8}	92	5.9×10^{-7}
QCD	5	$50 < \hat{p}_T < 80$	2.1×10^{7}	198	9.5×10^{-6}
QCD	6	$80 < \hat{p}_T < 120$	2.9×10^{6}	49	1.7×10^{-5}
QCD	7	$120 < \hat{p}_T < 170$	5.0×10^{5}	291	5.8×10^{-4}
QCD	8	$170 < \hat{p}_T < 230$	1.0×10^{5}	355	3.5×10^{-3}
QCD	9	$230 < \hat{p}_T < 300$	2.4×10^{4}	389	1.6×10^{-2}
QCD	10	$300 < \hat{p}_T < 380$	6.4×10^{3}	283	4.4×10^{-2}
QCD	11	$380 < \hat{p}_T < 470$	1.9×10^{3}	186	9.8×10^{-2}
QCD	12	$470 < \hat{p}_T < 600$	6.9×10^{2}	190	2.8×10^{-1}
QCD	13	$600 < \hat{p}_T < 800$	2.0×10^{2}	94	4.6×10^{-1}
QCD	14	$800 < \hat{p}_T < 1000$	3.6×10^{1}	89	2.5×10^{0}
QCD	15	$1000 < \hat{p}_T < 1400$	1.1×10^{1}	89	8.2×10^{0}
QCD	16	$1400 < \hat{p}_T < 1800$	1.1×10^{0}	39	3.7×10^{1}
QCD	17	$1800 < \hat{p}_T < 2200$	1.4×10^{-1}	38	2.6×10^{2}
QCD	18	$2200 < \hat{p}_T < 2600$	2.4×10^{-2}	41	1.7×10^{3}
QCD	19	$2600 < \hat{p}_T < 3000$	4.3×10^{-3}	5	1.2×10^{3}
QCD	20	$3000 < \hat{p}_T < 3500$	8.4×10^{-4}	4	4.7×10^{3}
QCD	21	$3500 < \hat{p}_T < 4000$	9.7×10^{-5}	4	4.1×10^{4}
$\mathrm{t\bar{t}}$	–	inclusive	4.9×10^{2}	3371	6.9

Table 10: Fully simulated Electro-Weak background samples used in this work.

Process	Bin	p_T range (GeV/c)	$\sigma_{\mathtt{LO}}$ (pb)	N (10^3 events)	L (fb^{-1})
W+jets	1	$0 < p_T(W) < 40$	1.1×10^5	365	3.3×10^{-3}
W+jets	2	$10 < p_T(W) < 100$	2.7×10^4	513	1.9×10^{-2}
W+jets	3	$25 < p_T(W) < 170$	1.0×10^4	759	7.5×10^{-2}
W+jets	4	$42.5 < p_T(W) < 300$	4.3×10^3	565	1.3×10^{-1}
W+jets	5	$75 < p_T(W) < 500$	1.2×10^3	270	2.2×10^{-1}
W+jets	6	$125 < p_T(W) < 800$	2.6×10^2	177	6.7×10^{-1}
W+jets	7	$200 < p_T(W) < 1400$	4.9×10^1	95	1.9×10^0
W+jets	8	$350 < p_T(W) < 2200$	4.9×10^0	70	1.4×10^1
W+jets	9	$550 < p_T(W) < 3200$	5.9×10^{-1}	47	7.9×10^1
W+jets	10	$800 < p_T(W) < 4400$	8.3×10^{-2}	16	1.9×10^2
Z+jets	1	$0 < p_T(Z) < 40$	3.2×10^4	198	6.3×10^{-3}
Z+jets	2	$10 < p_T(Z) < 100$	5.2×10^3	288	5.6×10^{-2}
Z+jets	3	$25 < p_T(Z) < 170$	1.5×10^3	396	2.7×10^{-1}
Z+jets	4	$42.5 < p_T(Z) < 300$	5.8×10^2	283	4.9×10^{-1}
Z+jets	5	$75 < p_T(Z) < 500$	1.6×10^2	147	9.1×10^{-1}
Z+jets	6	$125 < p_T(Z) < 800$	3.7×10^1	95	2.6×10^0
Z+jets	7	$200 < p_T(Z) < 1400$	7.0×10^0	44	6.3×10^0
Z+jets	8	$350 < p_T(Z) < 2200$	7.1×10^{-1}	26	3.6×10^1
Z+jets	9	$550 < p_T(Z) < 3200$	8.5×10^{-2}	20	2.4×10^2
Z+jets	10	$800 < p_T(Z) < 4400$	1.2×10^{-2}	8	6.8×10^2
WW+jets	–	inclusive	1.9×10^2	483	2.6
WZ+jets	–	inclusive	2.7×10^1	276	10.3
ZZ+jets	–	inclusive	1.1×10^1	478	43.0

B Comparison of ORCA with FAMOS

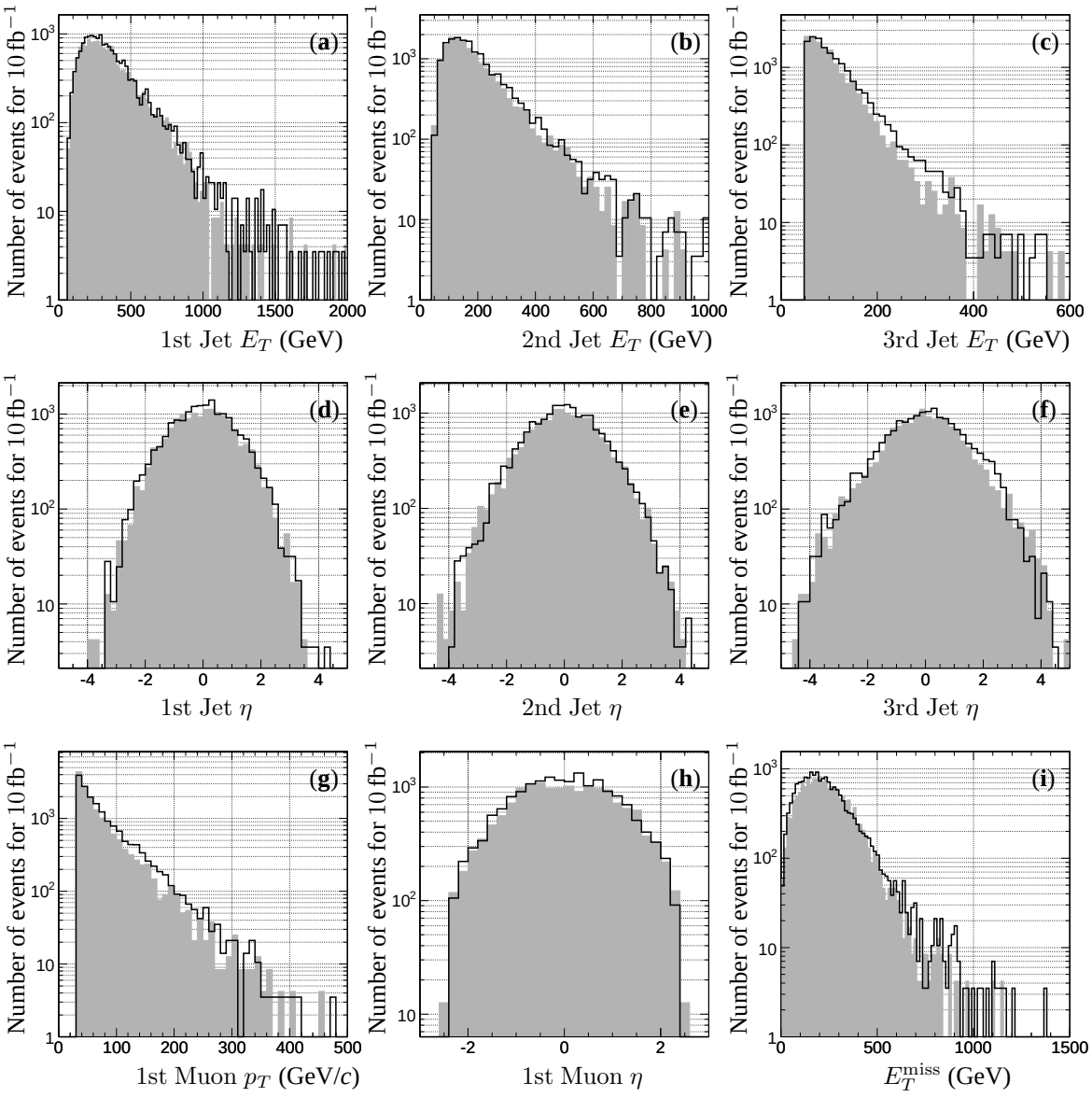

Figure 13: Comparison of FAMOS (shaded area) with ORCA (solid black line) for different reconstructed quantities used in the analyses. Only quality pre-selection cuts have been applied.

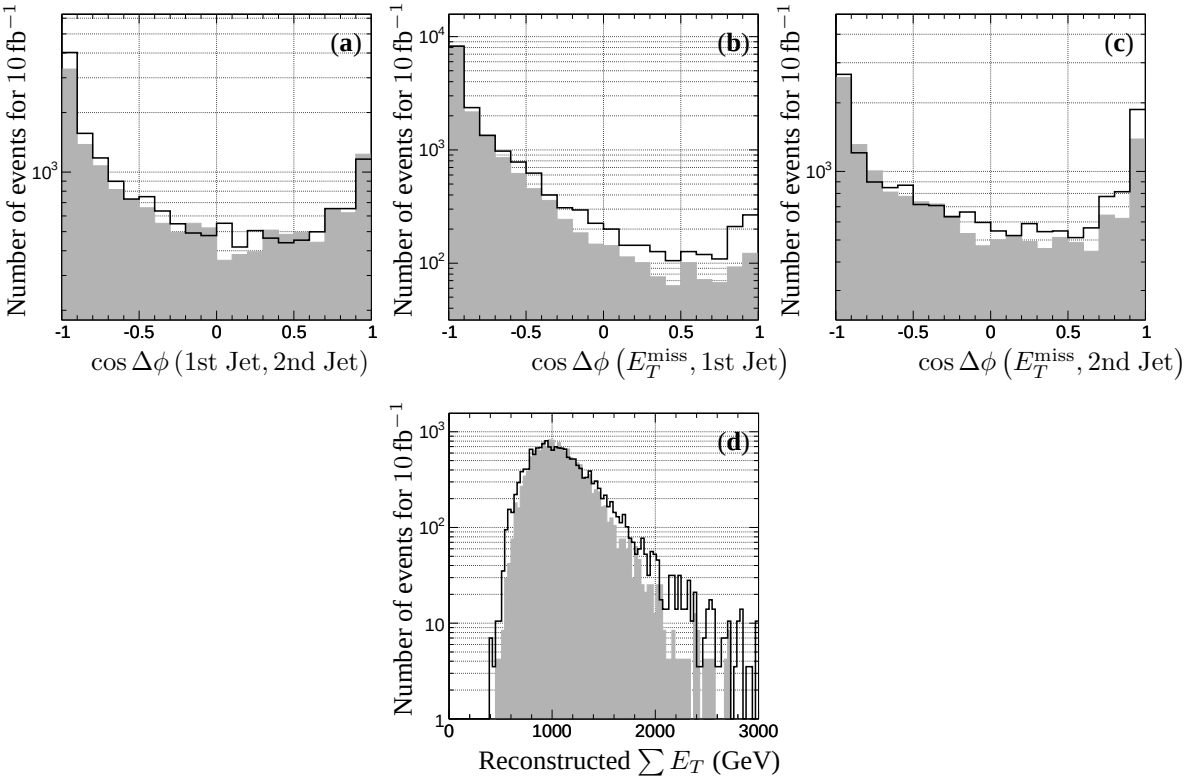

Figure 14: Comparison of FAMOS (shaded area) with ORCA (solid black line) for different reconstructed quantities used in this analysis. Only quality pre-selection cuts have been applied.

References

[1] D.N. Spergel, *et al* (WMAP Collaboration), *"First Year Wilkinson Microwave Anisotropy Probe (WMAP) Observations: Determination of Cosmological Parameters"*, **astro-ph/0302209**, Astrophys. J. Suppl. **148**, 175 (2003).

[2] V. Barger, C.E.M. Wagner, *et al., "Report of the SUGRA Working Group for Run II of the Tevatron"*, **hep-phy/0003154** (2000).

[3] LEPSUSYWG, ALEPH, DELPHI, L3 and OPAL experiments, *"LEP2 SUSY Working Group Web Page"*, http://lepsusy.web.cern.ch/lepsusy/ .

[4] R. Barate, *et al.*, (LEP Working Group for Higgs Boson Searches and ALEPH Collaboration and DELPHI Collaboration and L3 Collaboration and OPAL Collaboration), *"Search for the Standard Model Higgs Boson at LEP"*, **hep-ex/0306033**, Phys. Lett. **B565**, 61-75 (2003).

[5] A. Heister, *et al.*, (ALEPH Collaboration), *"Search for Charginos Nearly Mass Degenerate with the Lightest Neutralino in e^+e^- Collisions at Centre-of-Mass Energies up to 209 GeV"*, **hep-ex/0203020**, Phys. Lett. **B533**, 223-236 (2002).

[6] R. Barate, *et al.*, (ALEPH Collaboration), *"Search for Supersymmetric Particles in e^+e^- Collisions at $\sqrt{s}$ up to 202 GeV and Mass Limit for the Lightest Neutralino"*, **hep-ex/0011047**, Phys. Lett. **B499**, 67-84 (2001).

[7] V. Abazov, *et al* (D$\varnothing$ Collaboration), *"Search for Squark and Gluinos in Events with Jets and Missing Transverse Energy in $p\bar{p}$ Collisions at $\sqrt{s} = 1.96$ TeV"*, **hep-ex/0604029**, Phys. Lett. **B638**, 119-127 (2006).

[8] CMS Collaboration, *"CMS Physics Technical Design Report Volume 1: Detector Performance and Software"*, **CERN/LHCC 2006-001** (2006).

[9] H. Baer *et al., "Gluino-cascade-decay signature at the Fermilab Tevatron collider"*, Phys. Rev. **D41**, vol. 3 (1990).

[10] R. Barnett *et al., "Discovering supersymmetry with like sign dileptons"*, Phys. Lett. **B315**, 349 (1993).

[11] K. Matchev, D. Pierce, *"Supersymmetry Reach of the Tevatron via Trilepton, Like-Sign Dilepton and Dilepton plus Tau Jet Signatures"*, Phys. Rev. **D60**, 075004 (1999).

[12] J. Nachtman and D. Saltzberg and M. Worcester, (CDF Collaboration), *"Study of a like-sign dilepton search for chargino-neutralino production at CDF"* **hep-ex/9902010** (1999).

[13] CMS Collaboration, *"CMS, the Compact Muon Solenoid: Technical Proposal"*, **CERN/LHCC 1994-038** (1994).

[14] CMS Collaboration, *"The Magnet Project Technical Design Report"*, **CERN/LHCC 1997-010** (1997).

[15] CMS Collaboration, *"The Tracker Project Technical Design Report"*, **CERN/LHCC 1998-006** (1998), Addendum **CERN/LHCC 2000-016** (2000).

[16] CMS Collaboration, "*The Electromagnetic Calorimeter Technical Design Report"*, **CERN/LHCC 1997-033** (1997), Addendum **CERN/LHCC 2002-027** (2002).

[17] CMS Collaboration, *"The Hadron Calorimeter Technical Design Report"*, **CERN/LHCC 1997-031** (1997).

[18] CMS Collaboration, *"The Muon Project Technical Design Report"*, **CERN/LHCC 1997-032** (1997).

[19] J. Allison, *et al., "Geant4 Developments and Applications"*, IEEE Transactions on Nuclear Science, Vol. **53**, Issue 1, 270-278 (2006).

[20] H. Baer, F.E. Paige, S.D. Protopescu and X. Tata, *"ISAJET: a Monte Carlo Event Generator for pp, $\bar{p}p$, and e^+e^- Interactions"*, http://www.hep.fsu.edu/ isajet/ .

[21] T. Sjostrand, S. Mrenna and P. Skands, *"PYTHIA 6.4 Physics and Manual"*, **hep-ph/0603175** (2006).

[22] H. L. Lai, *et al*, (CTEQ Collaboration), *"Global QCD Analysis of Parton Structure of the Nucleon: CTEQ5 Parton Distributions"*, **hep-ph/9903282**, Eur. Phys. J. **C12**, 375-392 (2000).

[23] M.L. Mangano, *et al*, *"ALPGEN, a Generator for Hard Multiparton Processes in Hadronic Collisions"*, **hep-ph/0206293** (2002).

[24] S. Frixione and B.R. Webber, *"Matching NLO QCD Computations and Parton Shower Simulations"*, **hep-ph/0204244**, JHEP **0206**, 029 (2002).

[25] CMS Collaboration, *"The Trigger and Data Acquisition project, Volume I. The Level-1 Trigger, Technical Design Report"*, **CERN/LHCC 2000-038** (2000).

[26] CMS Collaboration, *"The Trigger and Data Acquisition project, Volume II. Data Acquisition and High-Level Trigger"*, **CERN/LHCC 2002-026** (2002).

[27] T. Affolder, *et al*, (CDF Collaboration), *"Search for Gluinos and Scalar Quarks in p anti-p Collisions at s**(1/2) = 1.8 TeV using the Missing Energy plus Multijets Signature"*, Phys. Rev. Lett. 88, 041801 (2002)

[28] S. Abdullin, *et al*, *"GARCON: Genetic Algorithm for Rectangular Cuts OptimizatioN. User's Manual for Version 2.0"*, **hep-ph/0605143** (2006).

[29] V. Abazov, *et al* (D∅ Collaboration), *"Search for mSUGRA in Single Electron Events with Jets and Large Missing Transverse Energy in p Anti-p Collisions at* $\sqrt{s} = 1.8\,TeV$*"*, **hep-ex/0205002**, Phys. Rev. **D66**, 112001 (2002).

[30] A. Pukhov, *et al*, *"CompHEP — a Package for Evaluation of Feynman Diagrams and Integration Over Multi-Particle Phase Space. User's Manual for Version 33"*, **hep-ph/9908288** (1999).

[31] S. Abdullin and F. Charles, *"Search for SUSY in (Leptons +) Jets +* E_T^{miss} *Final States"*, **hep-ph/9811402**, **CMS Note 1998-073** (1998).